Supplementary information

An ultrahigh performance hybrid energy harvester leveraging the induced charge excitation strategy

This file includes:

Other supplementary information for this manuscript includes the following:

Supplementary Experimental Procedures

Fabrication of the electrodes:

The optimized TENG-electrodes in Sections 2.2–2.5 are fabricated by sequentially attaching the following layers: a 1 mm acrylic substrate (150 mm × 100 mm), a 1 mm PDMS film (150 mm × 100 mm), a 60 μm copper film with rounded corners (upper electrode: 140 mm × 93.5 mm; bottom electrode: 135 mm × 92 mm; corner radius: 10 mm; effective area: 0.013 m^2), and a 30 μm PVDF film (150 mm × 100 mm) are attached in order. The PDMS film functions as a buffer layer to ensure effective contact. A cross-sectional schematic diagram of TENG-electrodes is provided in Fig. S35. For the pump-electrode, a 100 μm aluminum film (200 mm × 200 mm) is attached to the acrylic substrate (200 mm × 200 mm). Photographs of the TENG-electrodes and pump-electrode can be found in Fig. S6.

Fabrication of the PMC:

The PMC is integrated on the printed circuit board. The diodes D_1, D_2, and D_p are 2CL72, while diodes D_3 and D_f are R5000. The PMC is encapsulated in the conformal coating to improve insulation performance.

Fabrication of the ICE-EVH prototype:

The ICE-EVH prototype consists of two wind cups, a rocker arm, an enclosed shell (170 mm × 170 mm × 150 mm), stacked TENG-electrodes, and a PMC (Fig. 6A and Fig. S31). The substrates of the enclosed shell and TENG-electrodes are 3D-printed using polylactic acid (PLA). A 100 μm aluminum film is attached to the enclosed shell, functioning as the pump-electrode. For the TENG-electrodes, a 30 μm PVDF film (140 mm × 140 mm), and a 60 μm aluminum film (130 mm × 130 mm; corner radius: 25 mm) are sequentially attached to the PLA substrate (140 mm × 140 mm). The stacked upper electrodes are fixed together by a PLA bracket and nylon screws, ensuring effective and synchronized contact with the bottom electrodes. PTFE tapes are adhered to the wirings of TENG-electrodes to prevent air discharge.

The high-voltage and vibration experimental platform:

Similar to our previous works, the experimental platform mainly comprises a high-voltage transformer (YDTW-10/100), a steel-stranded aluminum wire, two insulating supports, and a grounded steel transmission tower. During the experiment, the output voltage of the high-voltage transformer reached an RMS value of 63.5 kV, simulating the single-phase 110 kV transmission line. Other key parameters, including conductor diameter, and insulation distance comply with IEEE and IEC standards for high-voltage transmission systems, ensuring a realistic replication of the electromagnetic environment. Notably, a minimum safety distance of 1.5 meters must be maintained during high-voltage experiments. After the experiment, all capacitive devices must be fully discharged and properly grounded before any subsequent experimental operations. In sections 2.2–2.5, a linear motor (Linmot E1200) was employed to provide standardized and tunable vibrations. In section 2.6, an air blower was employed to simulate airflow.

Characterization and measurement:

The voltage, current, transferred charge, and capacitor charging curves were measured using an electrometer (Keithley 6514) with a digital multimeter (Keithley DMM6500). For a voltage higher than 200 V, it was measured using an oscilloscope (Tektronix TBS 2000B) with a high-voltage probe (Pintech P6039A with 900 MΩ input resistance) or an electrostatic voltmeter (Trek 341B). For a current higher than 20 mA, it was measured using a current monitor (Pearson 6595). Measurement devices for other physical quantities are summarized in Table S5. The models of all commercial electronic devices are summarized in Table S4. The finite element simulation was completed by using COMSOL Multiphysics 5.6.

Supplementary Figures 1-35

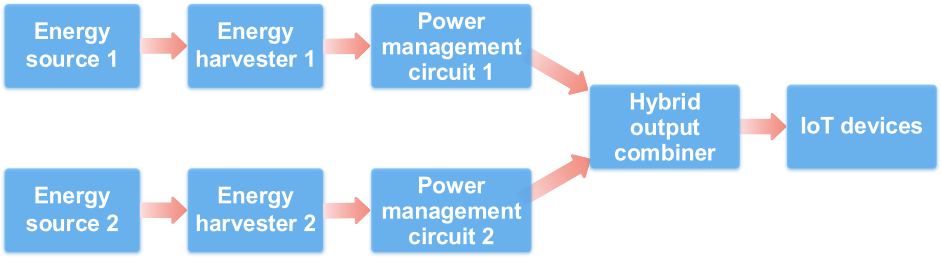

Figure S1. Overall system of conventional hybrid energy harvesters.

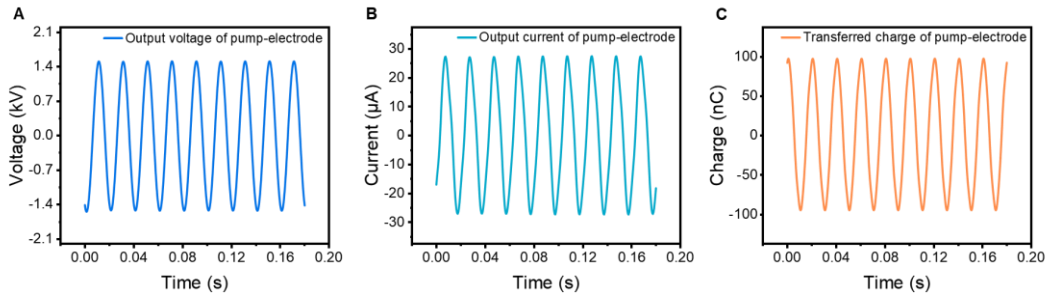

Figure S2. Original output of the pump-electrode.

(A) Open-circuit voltage.

(B) Short-circuit current.

(C) Short-circuit transferred charge.

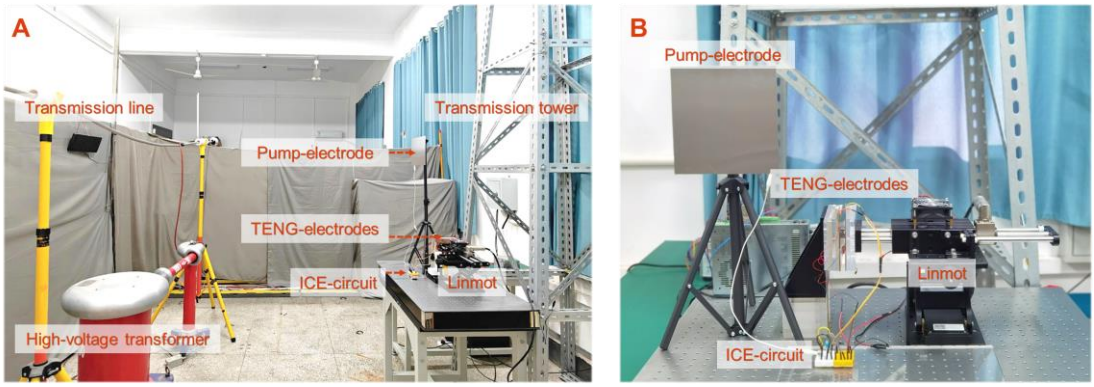

Figure S3. Photographs of the experimental platform.
(A) Panoramic view of the experimental platform.
(B) Photograph of the vibration experimental platform.

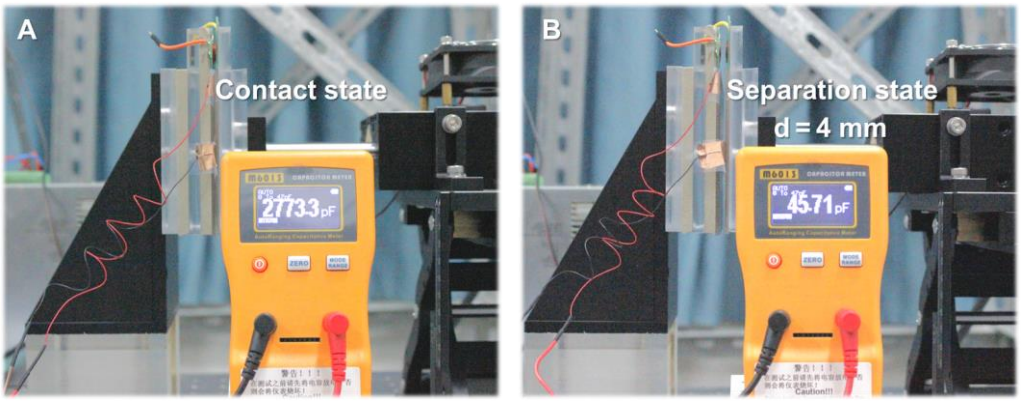

Figure S4. Parasitic capacitances of TENG-electrodes at contact and separation states.

(A) Contact state.

(B) Separation state.

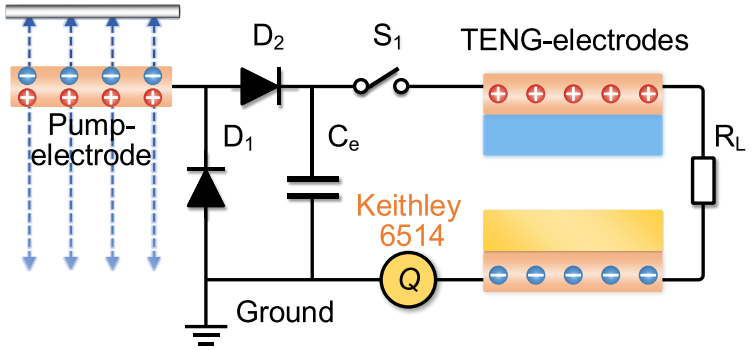

Figure S5. Measurement circuit diagram of transferred charge Q_p.

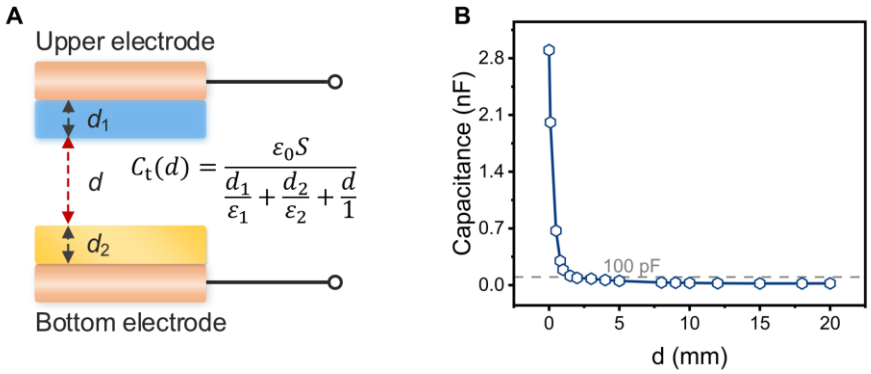

Figure S6. Relationship between parasitic capacitance C_t and distance d of TENG-electrodes.

(A) Schematic diagram of the TENG-electrodes.

(B) Capacitance of C_t at different distances d.

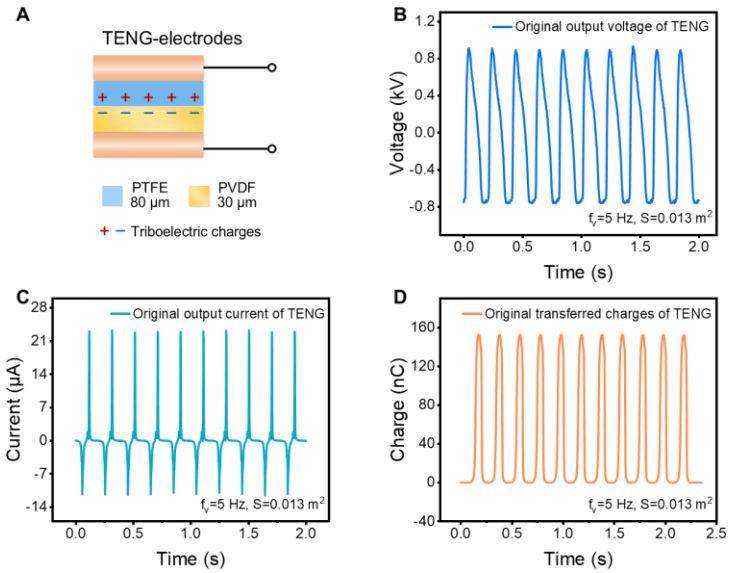

Figure S7. Original output of the TENG-electrodes without induced charge excitation.

(A) Structure schematic of the original TENG-electrodes.

(B)–(D) Original output of the TENG-electrodes.

(B) Open-circuit voltage.

(C) Short-circuit current.

(D) Short-circuit transferred charge. The surface of PTFE film was roughened to enhance the triboelectric charge density.

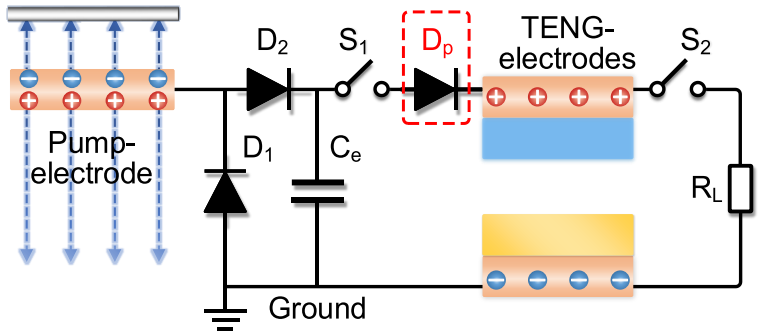

Figure S8. Circuit diagram of the ICE-circuit with the diode D_p.

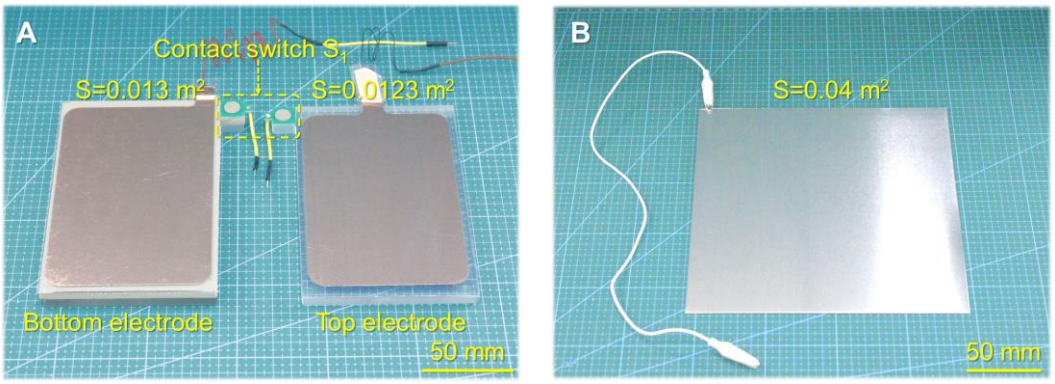

Figure S9. Photographs of the TENG-electrodes, switch S_1, and pump-electrode.
(A) Photograph of the TENG-electrodes and the switch S_1.
(B) Photograph of the pump-electrode.

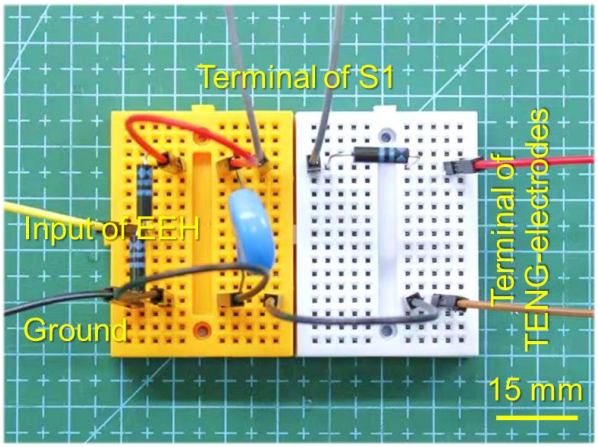

Figure S10. Photograph of the induced charge excitation circuit.

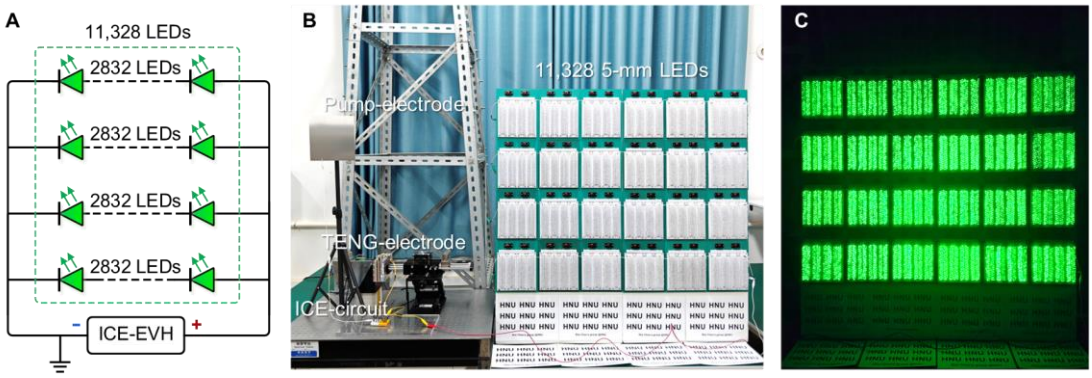

Figure S11. Photographs and circuit diagram of 11 328 LEDs.

(A) Circuit diagram of 11 328 LEDs connected in series and parallel.

(B) Photograph of the experiment setup.

(C) Light up 11 328 LEDs by ICE-EVH at 5 Hz.

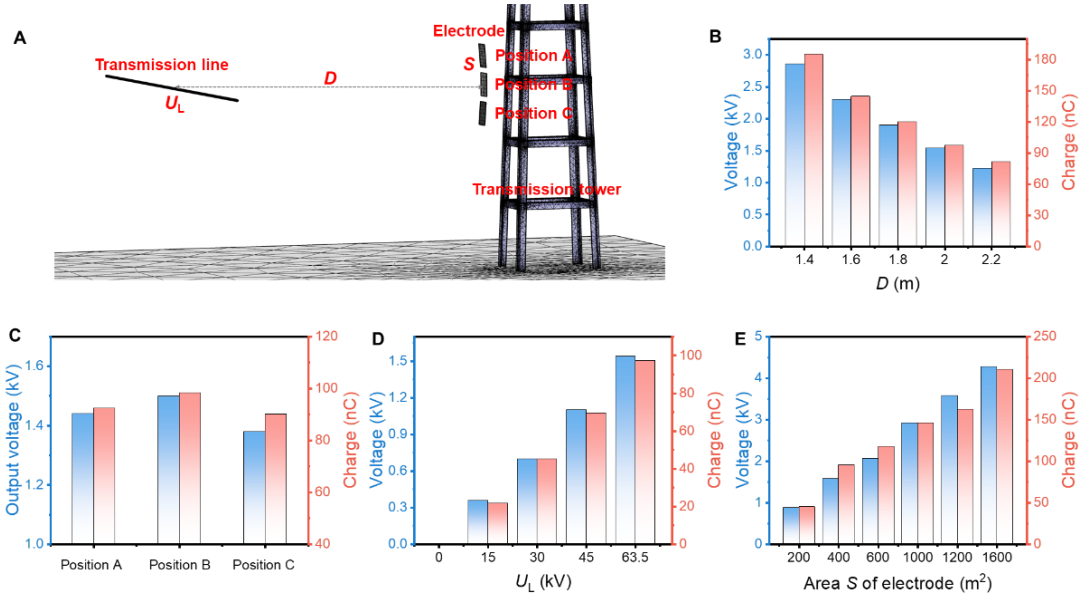

Figure S12. Factors affecting the output of the electric-field energy harvester.
(A) Schematic diagram of the parameters.
(B)–(E) Influences of distance D, position, operating voltage U_L, and electrode area S.

Generally, EEH's output is determined by the parasitic capacitance C_q between the transmission line and the pump-electrode, and the electric-field strength near the electrode (Note S1).[1,2] Increasing D reduces both the electric field strength near the pump-electrode and C_q, resulting in decreased output (Fig. S12B). Different installation positions also result in different outputs. The output voltage reaches its maximum when the pump-electrode is directly aligned with the transmission line (Fig. S12C). Increasing U_L enhances the electric field strength around the electrode, thereby enhancing the output (Fig. S12D). A larger electrode area S increases C_q, thereby improving the output (Fig. S12E).

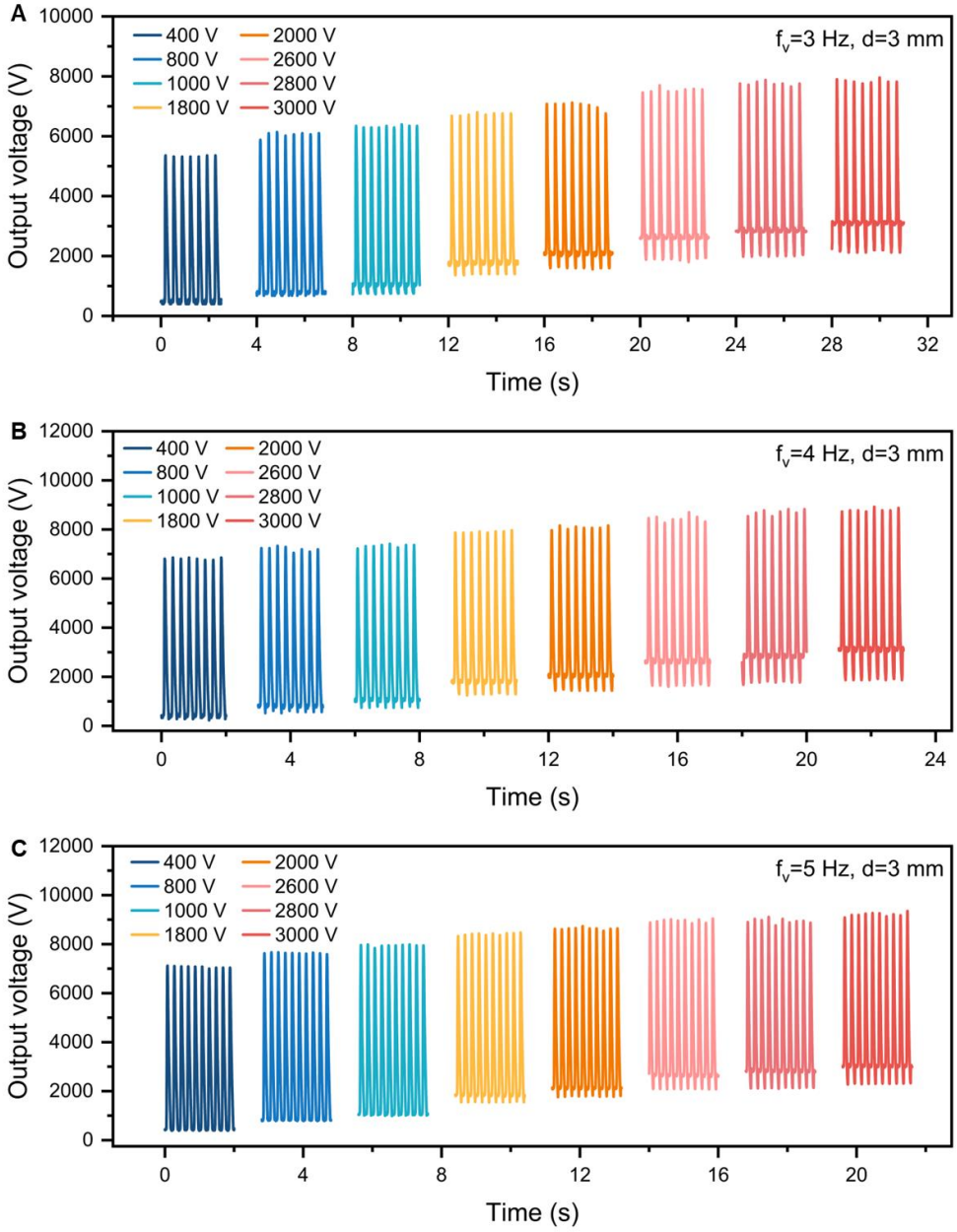

Figure S13. Output voltage curves of ICE-EVH at different excitation voltages and vibration frequencies.

(A) 3 Hz.

(B) 4 Hz.

(C) 5 Hz.

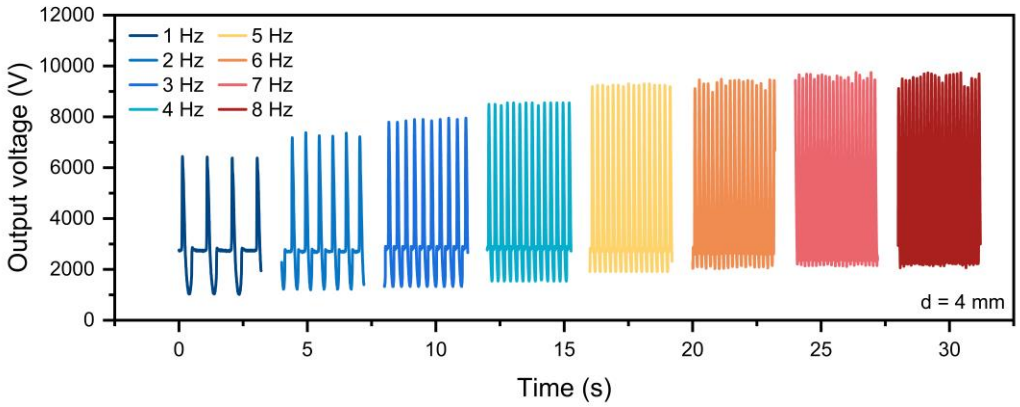

Figure S14. Output voltage curves of ICE-EVH at different vibration frequencies.

As the vibration frequency f_v of TENG increases, the time interval for each vibration cycle decreases, leading to reduced charge decay (Note S4). Therefore, as f_v increases from 1 Hz to 6 Hz, the output voltage rises significantly from 6.4 kV to 9.4 kV. However, when f_v exceeds 6 Hz, the charge decay becomes minimal, and further increases in frequency lead to marginal improvements.

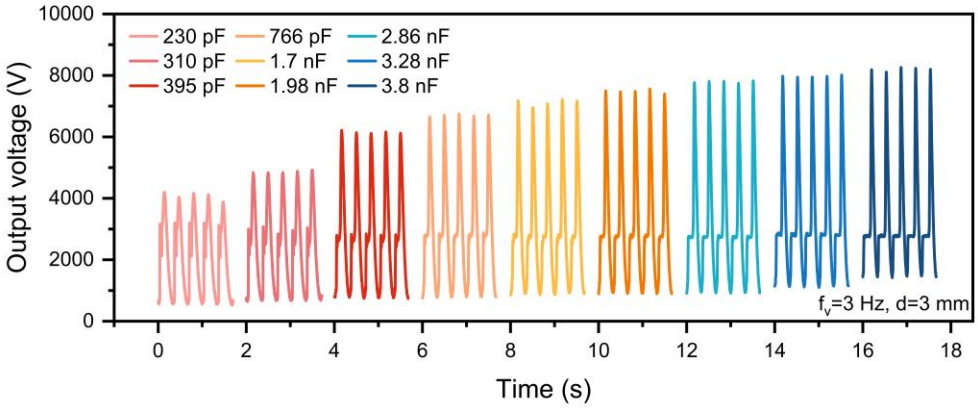

Figure S15. Output voltage curves of ICE-EVH with different C_{t_max}.
When 220 pF < C_{t_max} < 2 nF, the output voltage increases significantly with C_{t_max}. When C_{t_max} exceeds 2 nF, the enhancement is moderate.

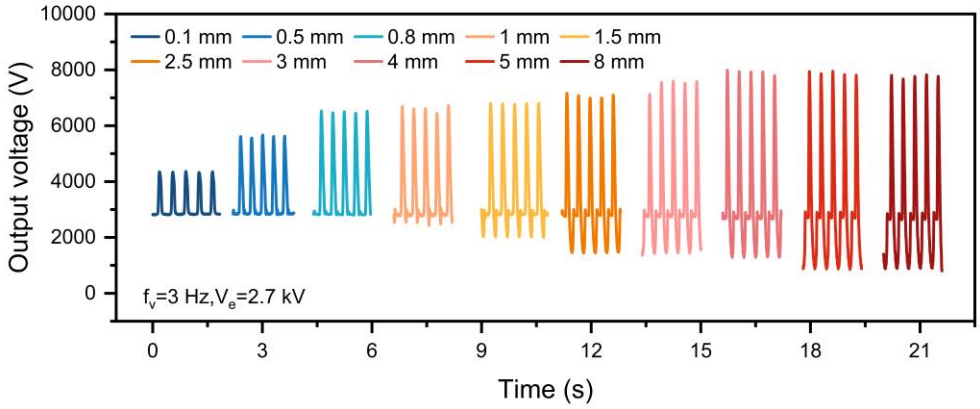

Figure S16. Output voltage curves of ICE-EVH with different *d* of TENG-electrodes.

When 0.1 mm < *d* < 4 mm, increasing *d* leads to a significantly decreased C_{t_min} (Fig. S6). According to equation 4 in the manuscript, the harvested mechanical energy during the separation process increases. Therefore, the output voltage significantly increases from 4.3 kV to 7.6 kV. However, when *d* > 4 mm, changes in C_{t_min} become minimal, leading to negligible variations in output voltage.

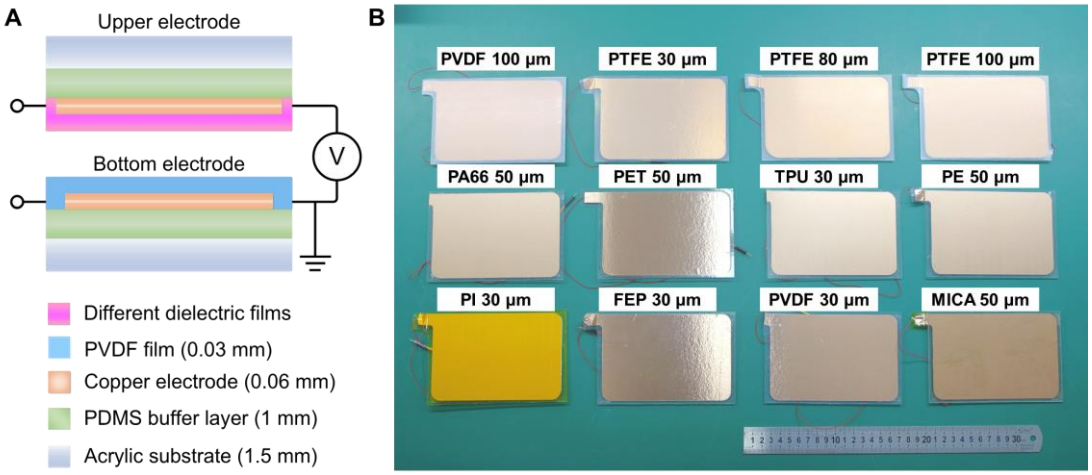

Figure S17. Photograph of TENG-electrodes prototypes with different dielectric materials.

(A) Cross-sectional schematic diagram of TENG-electrodes and measurement circuit.

(B) Photograph of different TENG-electrodes prototypes.

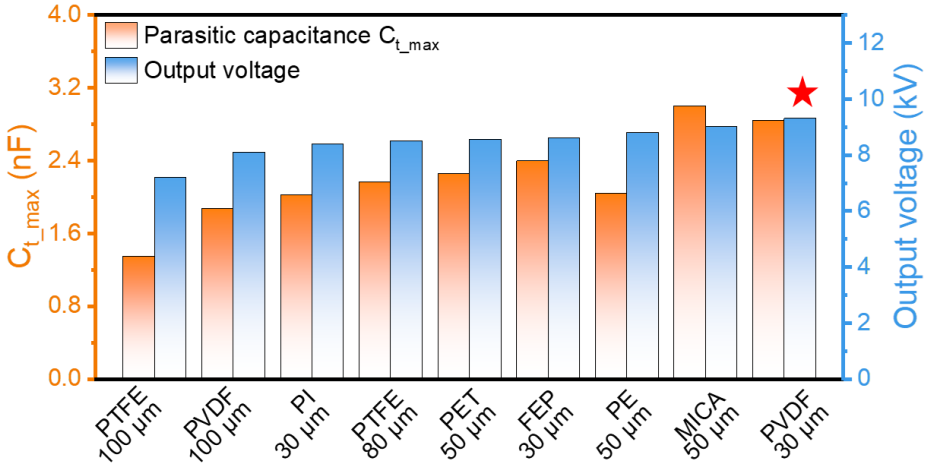

Figure S18. Parasitic capacitance and output voltage of TENG-electrodes prototypes with different dielectric films.

Generally, the output voltage increases with the maximum parasitic capacitance C_{t_max}, C_{t_max}, as higher C_{t_max} results in increased pumped charge Q_p and higher charge density. However, for materials such as PE and MICA, exceptions occur due to their different dielectric charge leakage characteristics.[3] A smaller dielectric charge leakage leads to reduced charge decay and higher charge density, thereby increasing the output voltage. Experimental results demonstrate that TENG-electrodes with two 30 μm PVDF films exhibit the optimal output performance.

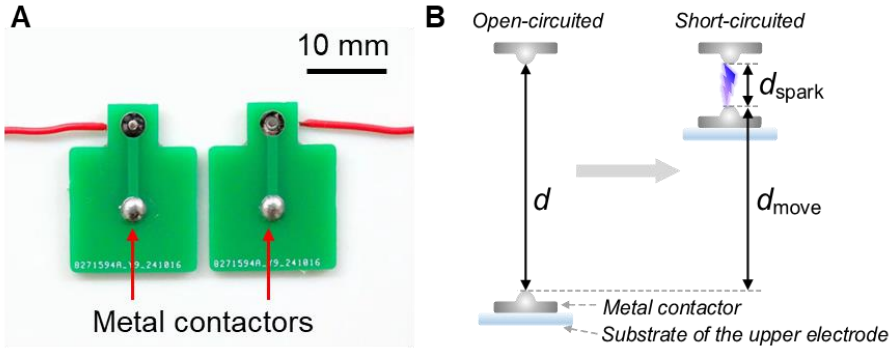

Figure S19. Photograph and structure diagram of switch S_2.

(A) Photograph of switch S_2.

(B) Structure diagram of switch S_2.

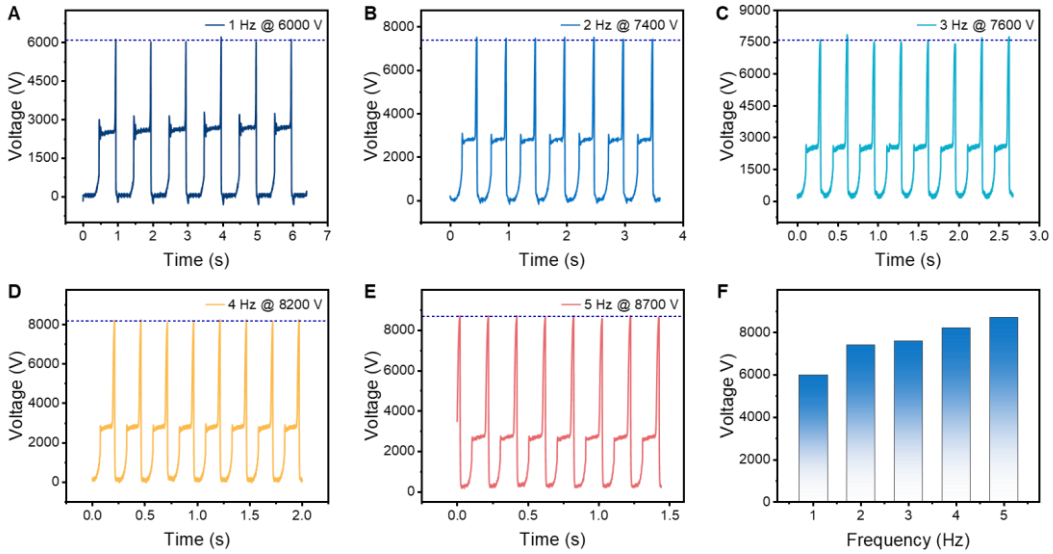

Figure S20. Discharge voltage curves and turn-on voltages of S_2 at different vibration frequencies.

(A)–(E) Discharge voltage curves of S_2 at different vibration frequencies.

(F) Comparison of the turn-on voltages of S_2 at different vibration frequencies.

As the vibration frequency increases from 1 to 5 Hz, the turn-on voltage of switch S_2 rises correspondingly, consistent with the output voltage trends observed in Fig. 3b and Fig. S14.

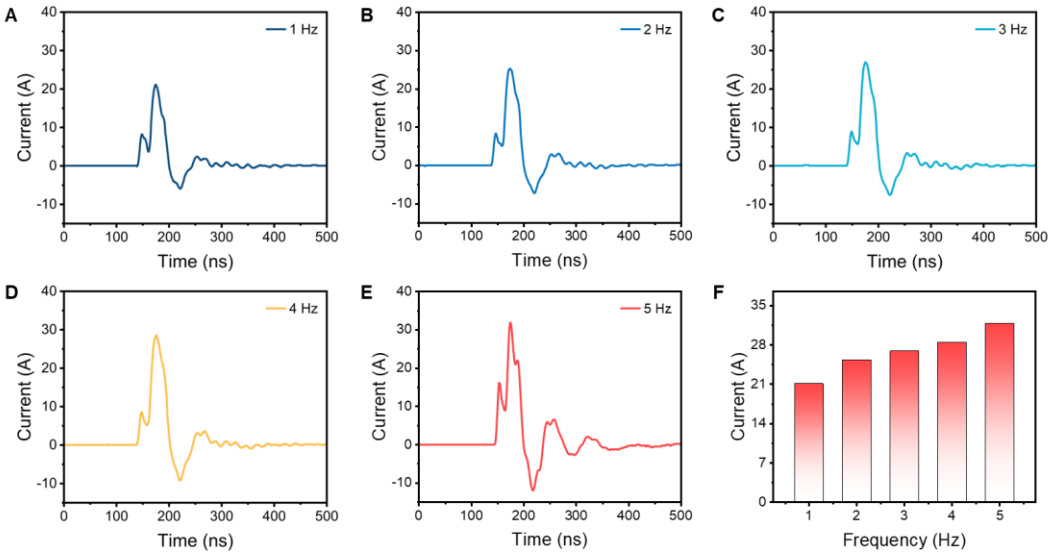

Figure S21. Discharge current curves of S_2 at different vibration frequencies.
(A)–(E) Discharge current curves of S_2 at different vibration frequencies.
(F) Comparison of discharge current at different vibration frequencies.

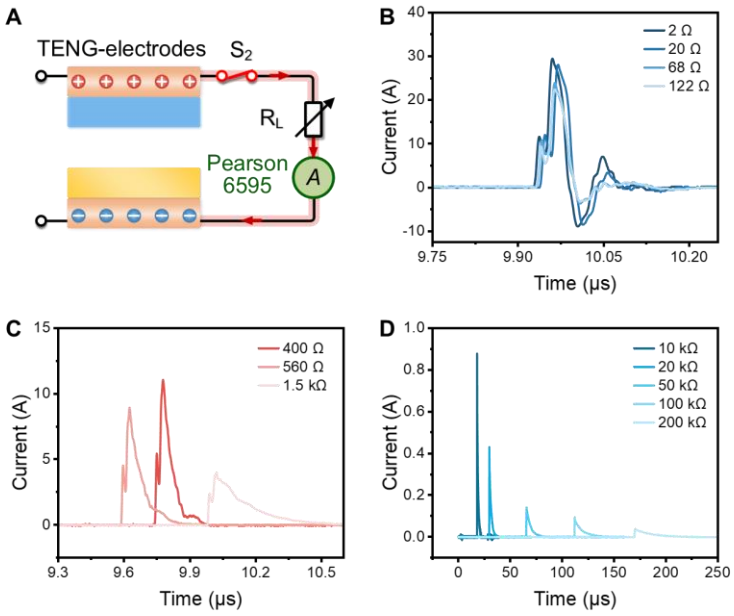

Figure S22. Output current curves at different resistive loads.

(A) Measurement circuit diagram of output current.

(B)–(D) Output current curves at different resistive loads. As the resistance of R_L increases, the hindrance to charge transfer gradually increases. Consequently, the peak value of the discharge current decreases gradually, while the pulse width of the waveform expands.

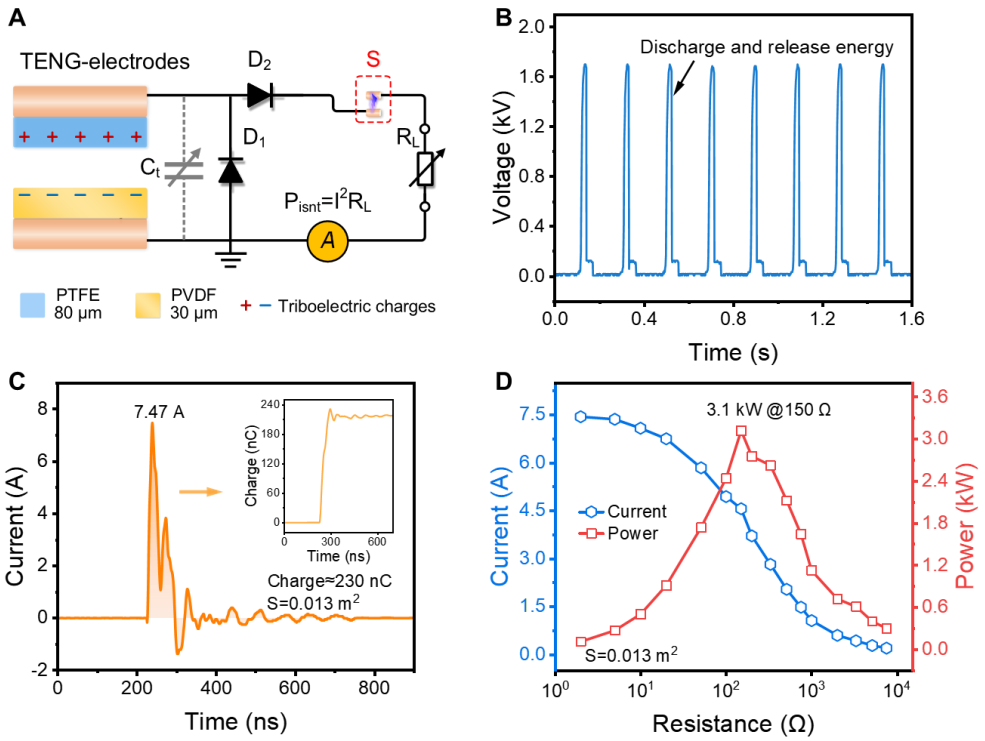

Figure S23. Instantaneous output power of the TENG prototype.

(A) Power management circuit for the TENG prototype.

(B) and (C) Discharge voltage and current waveforms of the TENG prototype after energy management.

(D) Output current and instantaneous power at different resistive loads.

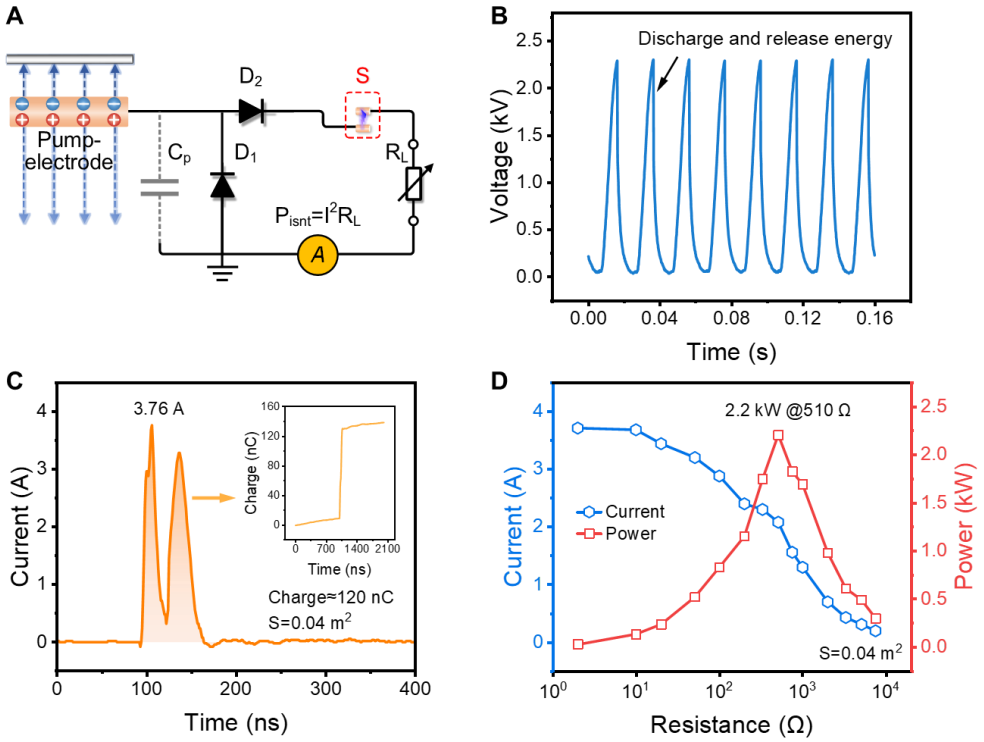

Figure S24. Instantaneous output power of the EEH prototype.

(A) Power management circuit for the EEH prototype.

(B) and (C) Discharge voltage and current waveforms of the EEH prototype after energy management.

(D) Output current and instantaneous power at different resistive loads.

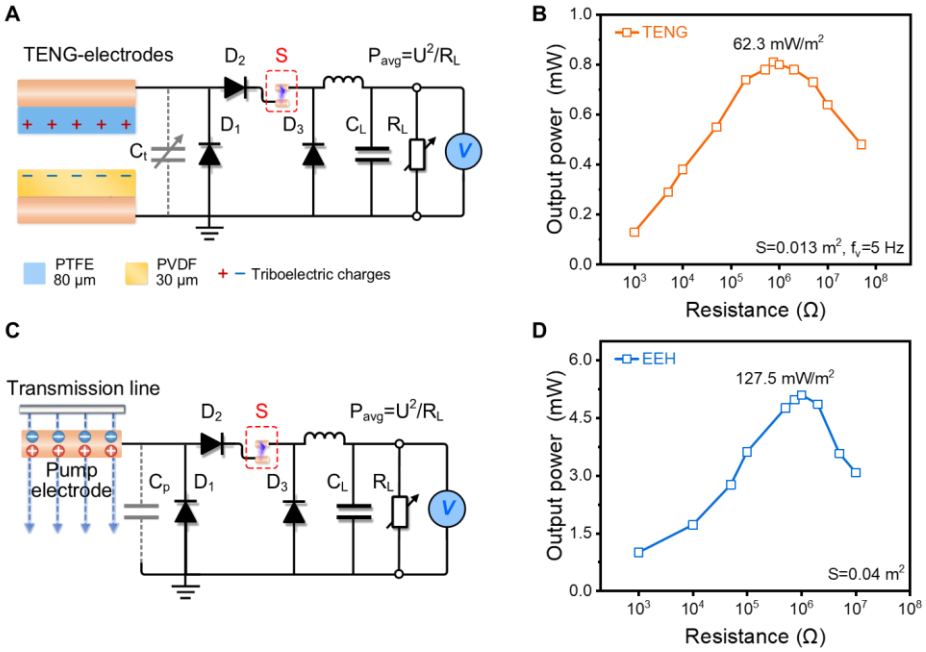

Figure S25. Average power densities for the TENG and EEH prototypes.
(A) Power management circuit for the TENG prototype.
(B) Average power density of the TENG prototype.
(C) Power management circuit for the EEH prototype.
(D) Average power density of the EEH prototype.

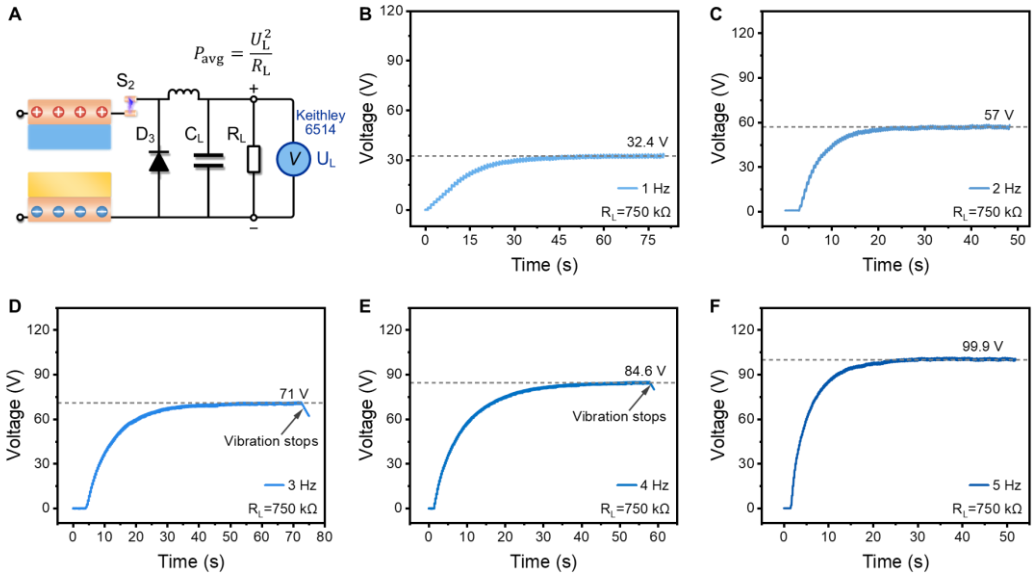

Figure S26. DC output voltage and average output power of ICE-EVH at different vibration frequencies.

(A) Measurement circuit diagram.

(B)–(F) DC output voltage at different vibration frequencies.

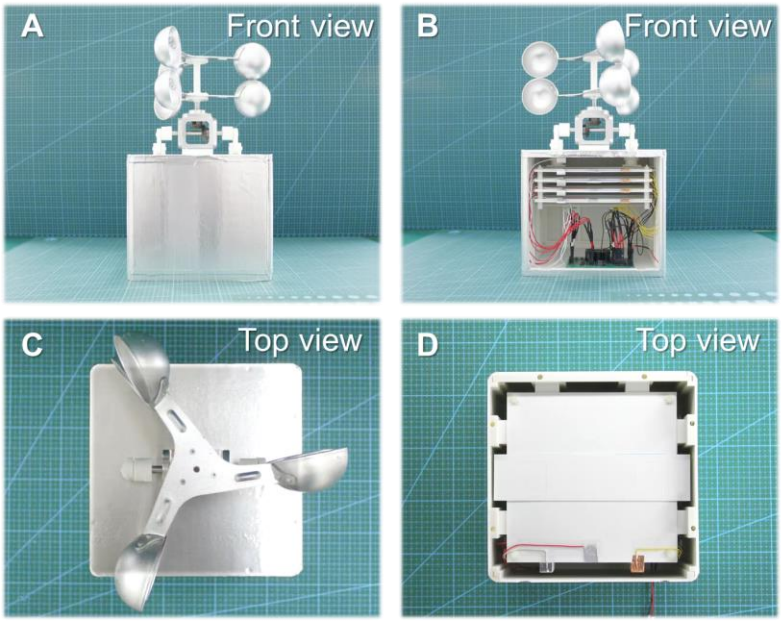

Figure S27. Photographs of the ICE-EVH prototype.
(A) and (B) Front view.
(C) and (D) Top view.

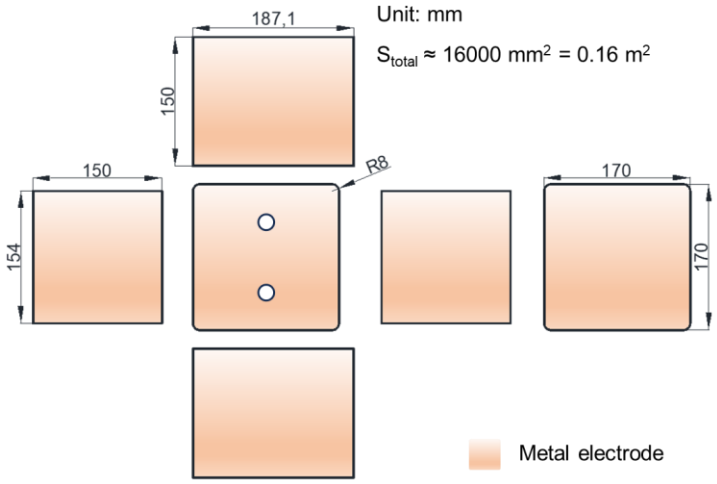

Figure S28. Dimensions of the pump-electrode integrated in the enclosed shell.

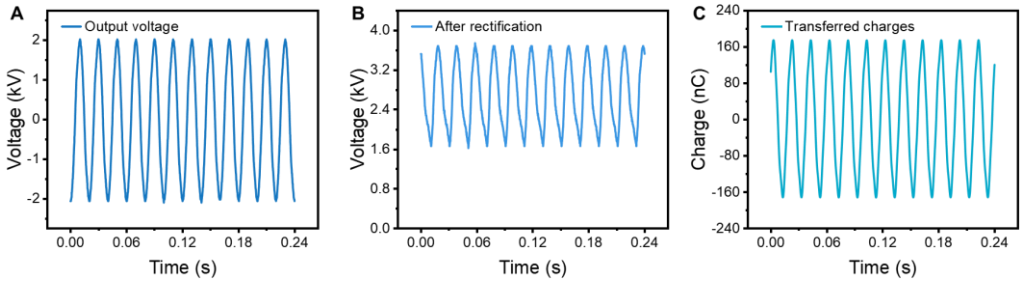

Figure S29. Output of the pump-electrode in the ICE-EVH prototype.

(A) Output voltage of the pump-electrode.

(B) Output voltage after the self-doubled rectification.

(C) Transferred charges of the pump-electrode.

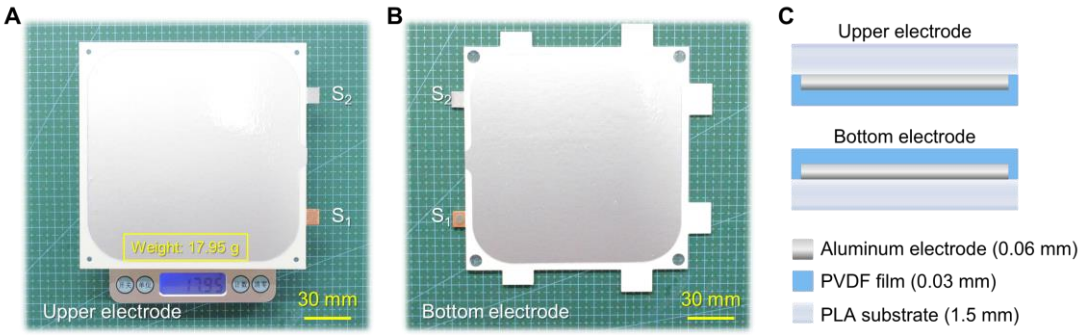

Figure S30. Photographs of the TENG-electrodes.

(A) Photograph of the upper electrode. The effective area of the electrode is 0.0163 m^2. The substrate is PLA (Bambu PLA basic) with a thickness of 0.52 mm. A 0.06 mm aluminum film is utilized as the metal layer instead of the copper film to reduce weight. The total weight of the upper electrode is only 18 g, which allows for low start-up wind speed.

(B) Photograph of the bottom electrode.

(C) Cross-sectional schematic diagram of TENG-electrodes in the prototype.

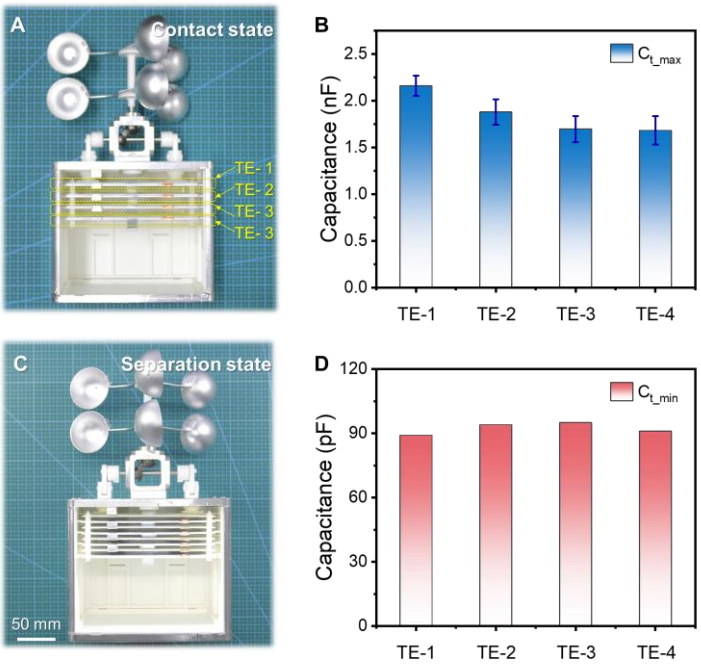

Figure S31. Parasitic capacitance of the stacked TENG-electrodes in the ICE-EVH prototype.

(A) Photograph of the stacked TENG-electrodes at the contact state.

(B) Parasitic capacitance of the stacked TENG-electrodes at the contact state.

(C) Photograph of the stacked TENG-electrodes at the separation state.

(D) Parasitic capacitance of the stacked TENG-electrodes at the separation state.

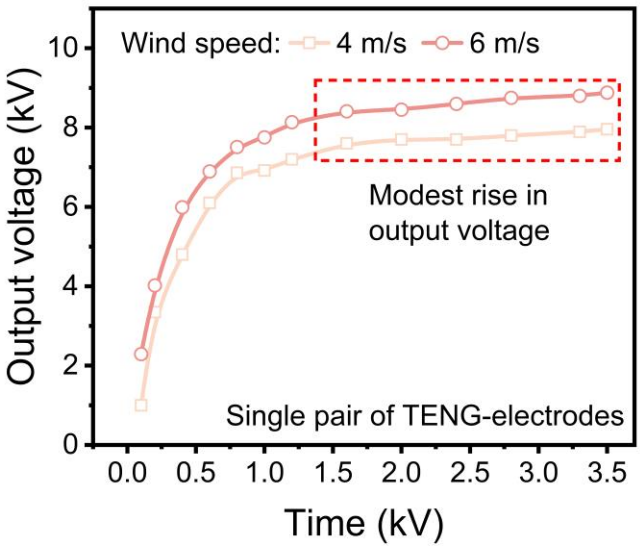

Figure S32. Output voltage of the ICE-EVH prototype at different excitation voltages.

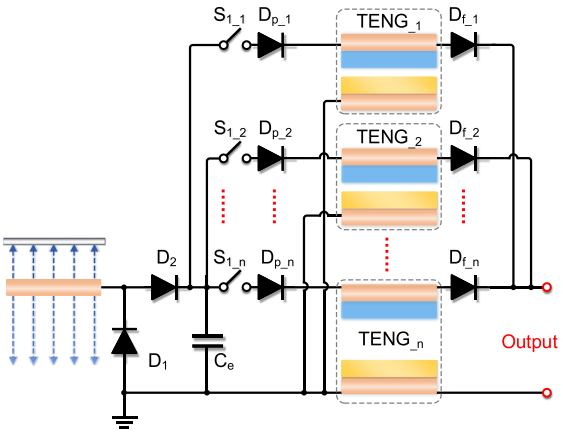

Figure S33. Circuit diagram for the stacked TENG-electrodes.

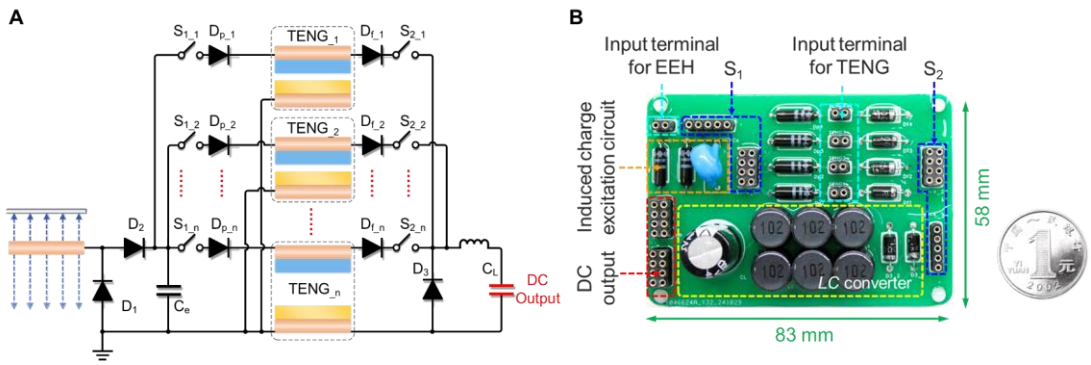

Figure S34. Circuit diagram and photograph of the multi-path PMC.

(A) Circuit diagram of the multi-path PMC for stacked TENG-electrodes.

To prevent interference caused by different output voltages among TENG-electrodes, an anti-backflow diode D_f was placed after each TENG-electrodes.

(B) Photograph of the multi-path PMC for stacked TENG-electrodes.

The PCB board and electronic components were coated with conformal coating to improve insulation performance.

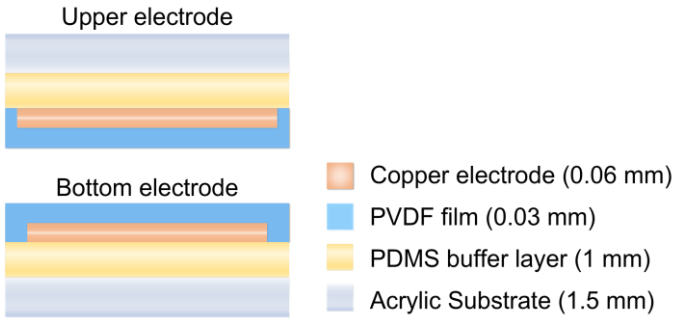

Figure S35. Cross-sectional schematic diagrams of TENG-electrodes.

Supplementary Tables 1-5

Table S1. Comparison of ICE-EVH with recently reported CS-TENGs, EEHs, and other representative hybrid energy harvesters.

Ref.	Energy source	Category	Peak power density	Average power density
Guo et al. (2023)[4]	Vibration energy	CS-TENG	3.55 kW/m^2	101.8 mW/m^2
Zeng et al. (2020)[2]	Electric-field energy	EEH	/	124 mW/m^2
Zhou et al. (2024)[5]	Electric-field energy	EEH	/	242 mW/m^2
Wang et al. (2021)[6]	Vibration energy	CS-TENG	11.13 kW/m^2	249 mW/m^2
Gao et al. (2023)[7]	Vibration energy	CS-TENG	7.056 kW/m^2	282.3 mW/m^2
Wang et al. (2021)[8]	Vibration energy	CS-TENG	10.9 kW/m^2	291 mW/m^2
Hu et al. (2024)[1]	EEH	EEH	495 kW/m^2 (previous record)	483 mW/m^2
Cao et al. (2024)[9]	Vibration energy	CS-TENG	/	509 mW/m^2 (previous record)
Cheng et al. (2013)[10]	Vibration energy	CS-TENG	360 kW/m^2	/
Shen et al. (2023)[11]	Mechanical energy	Piezo-tribo nanogenerator	188 mW/m^2	66.8 mW/m^2
Hu et al. (2024)[12]	Electric-field and vibration energy	CS-TENG and EEH	2.23 W/m^2	29.3 mW/m^2
Bao et al. (2023)[13]	Solar and raindrop energy	Solar panel and TENG	3.71 mW/m^2	/
Ye et al. (2023)[14]	Solar and raindrop energy	Solar panel and TENG	40.8 mW/m^2	/
Liu (2024)[15]	Wind and water wave energy	CS-TENG	2.9 W/m^2	140 mW/m^2
This work	Electric-field and vibration energy	ICE-EVH	**5146 kW/m^2** (10.4 times the previous record)	**1015 mW/m^2** (2 times the previous record)

Note: The power density of each energy harvester was determined as the ratio of output power P to electrode area S. For charge-excitation-based TENG, the power density was calculated using the metal electrode area of the main-TENG.

Table S2. Comparison of output performance among EEH, TENG, and ICE-EVH.

Output performance	Voltage (kV)	Current (A/m^2)	Charge density ($\mu C/m^2$)	Instantaneous power density (kW/m^2)	Average power density (mW/m^2)
TENG	0.91	574.6	11.7	240	62.31
EEH	1.5	94	2.43	55.16	127.5
"TENG+EEH"	2.41	668.6	14.13	295.16	189.81
ICE-EVH	9.2	2400	83.8	5146	1015
"ICE-EVH / (TENG+EEH)"	3.82 times	3.59 times	5.93 times	17.43 times	5.34 times

Note: The hybrid efficiency is calculated as the ratio of ICE-EVH's output to the sum of TENG and EEH outputs (the last row in Table S2).[11] The results show that ICE-EVH outperforms the sum of EEH's and TENG's individual outputs by a factor of 3.59–17.43, demonstrating its superior "1+1 > 2" hybrid performance.

Table S3. List of Abbreviations in the manuscript.

Abbreviations and symbols	Full name /Explanation
AC	Alternating current
EEH	Electric-field energy harvester
HEH	Hybrid energy harvester
ICE-EVH	Induced charge excitation based electric-field and vibration hybrid energy harvester
ICE-circuit	Induced charge excitation circuit
PMC	Power management circuit
TENG	Triboelectric nanogenerator
TE	TENG-electrodes
C_t	Parasitic capacitance of the TENG-electrodes
C_{t_max}	Maximum parasitic capacitance of the TENG-electrodes at the contact state
C_{t_min}	Minimum parasitic capacitance of the TENG-electrodes at the separation state
C_p	Parasitic capacitance between the pump-electrode and the ground
C_p	Parasitic capacitance between the pump-electrode and the transmission line
E	Energy stored in the capacitor
ΔE	Output energy per cycle
F	Mechanical force
f_v	Vibration frequency of TENG-electrodes
Q_p	Pumped charges per cycle
S	Area of the metal electrode
V_{oc_p}	Open-circuit output voltage of the pump-electrode

Table S4. List of commercial electric devices used in the manuscript.

Electric devices	Model	Operating voltage	Rated power consumption
Wireless camera	Huabao 720p	2.6–5 V	≈ 0.8 W (Start-up and stand-by) ≈ 1 W (Wireless communication) ≈ 1.4 W (Taking pictures)
Hygro-thermograph	Lanjun CX-260D	1.5 V	≈ 90 μW (Start-up) ≈ 25 μW (Typical) ≈ 60 μW (Activated, every 10 seconds)
Lamps	XJP 4640-4C30B	12 V	100 W

Table S5. List of measurement devices used in the manuscript.

Parameter	Measurement devices	Model
Voltage (0–200 V)/ Current (0–20 mA)/ Charge (0–20 μC)	Electrometer	Keithley 6514
Voltage (> 200 V)	Electrostatic voltmeter/ High voltage prototype	Trek 341B/ Pintech 6039A
Current (> 20 mA)	Current transformer	Pearson 6595
Data acquisition	Digital multimeter/ Oscilloscope	Keithley DMM6500/ Tektronix TBS2000B
Temperature and humidity	Hygro-thermograph	Lanjun CX-260D
Thickness and displacement	Vernier caliper	Teama CDE110MW
Capacitance of C_t	Capacitance meter	Jingyan M6013
Wind speed	Anemometer	UNI-T UT363BT

Supplemental Notes 1-9

Note S1 Working principle of electric-field energy harvester.

The pump-electrode and transmission line form a low-potential electric-field energy harvester (EEH), and its diagram is shown in Fig. N1A. According to electromagnetic theory, free charges in the metal electrode move directionally and accumulate on the metal surface due to the external electric field. These accumulated charges are defined as induced charges (Fig. N1A). When the electrode is connected to the ground through an external circuit, the time-varying electric field drives free charges to flow in and out of the ground periodically (Fig. N1B i–ii). An AC output current is generated during this process, converting the electric-field energy into electricity.

The equivalent circuit of the low-potential EEH with the ICE-circuit is shown in Fig. N1C, where C_q and C_p represent the parasitic capacitances between the pump-electrode and the transmission line, as well as the ground, respectively. C_q and C_p are typically less than 100 pF.[2] ICE-circuit is connected in parallel with C_p. The displacement current I_{out} flowing through the metal electrode is given by:

$$I_{out} = \frac{U_L}{Z_q + Z_p} \tag{N1}$$

where Z_q denotes the equivalent impedance of C_q, and Z_p represents the impedance of the parallel combination of C_p and the ICE-circuit. Since the ICE-circuit includes a buffer capacitor C_e (~nF), Z_p is much smaller than Z_q. Thus, I_{out} can be calculated as:

$$I_{out} \approx \frac{U_L}{Z_q} = j\omega C_q U_L \tag{N2}$$

Consequently, the output of EEH in ICE-EVH system primarily depends on the parasitic capacitance C_q between the metal electrode and the transmission line, and the operating voltage U_L.

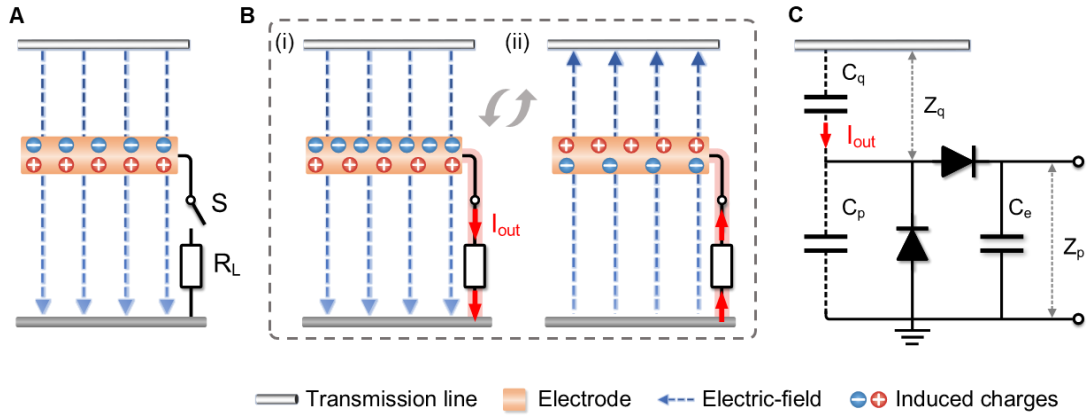

Figure N1. Working principle of electric-field energy harvester.
(A) Circuit diagram of the low-potential EEH.
(B) Working process of the EEH.
(C) Equivalent circuit of the EEH and the ICE-circuit.

Note S2 Working principle of TENG-based vibration energy harvester.

The fundamental working principles of a TENG are contact electrification and electrostatic induction. As illustrated in Fig. N2 i, when two dielectric films contact, opposite charges accumulate on the surfaces due to the contact electrification effect. In this initial state, there is no potential difference between the electrodes due to the electrostatic shielding effect.

When an external mechanical force separates the upper electrode from the bottom electrode, a potential difference develops between the electrodes (Fig. N2 ii). This potential difference drives free charges to flow through the external load, generating an output current. As the electrodes contact and separate periodically, an alternating current is generated in the external circuit (Fig. N2 ii–iv). Consequently, TENG can effectively convert mechanical vibration energy into electricity.

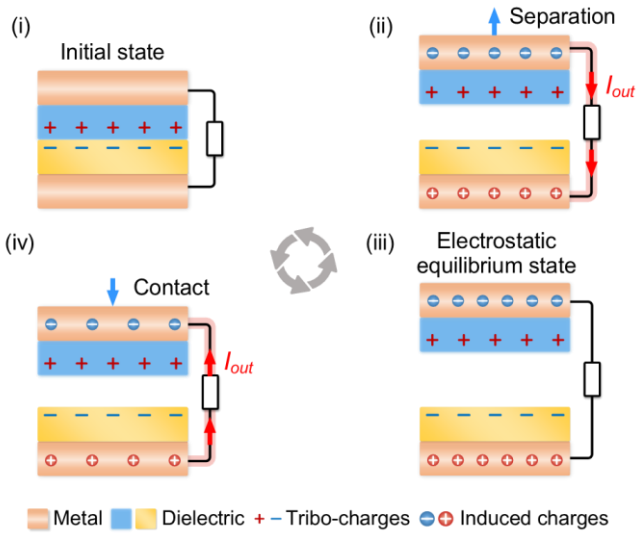

Figure N2. Working principle of TENG-based vibration energy harvester.

Note S3 The theoretical relationship between the output voltage and excitation voltage.

The working process and equivalent circuit model of ICE-EVH are shown in Fig N3. The first stage is the accumulation of induced charge (Fig. N3 i). The voltage across C_e gradually rises to V_e. Subsequently, the induced charge stored in C_e is pumped to C_t (Fig. N3 ii). At equilibrium state, the quantity of charge pumped in C_t is Q_p, which can be calculated as:

$$Q_p = \frac{C_e C_{t\_max}}{C_e + C_{t\_max}} V_e \tag{N3}$$

As the upper electrodes separate from the bottom one (Fig. N3 iii), the parasitic capacitance of the TENG-electrodes decreases from C_{t_max} to C_{t_min}. Theoretically, the voltage V_{out} across C_t after separation is:

$$V_{out} = \frac{Q_p}{C_{t\_min}} = \frac{C_e C_{t\_max}}{(C_e + C_{t\_max}) C_{t\_min}} V_e \tag{N4}$$

Therefore, if there is no charge decay in the TENG-electrodes, the output voltage V_{out} should be directly proportional to the excitation voltage V_e. However, charge decay is a common challenge in charge-excitation-based TENGs, and higher excitation voltages lead to more severe charge decay.[3] Consequently, as shown in Fig. 3A and Fig. S32, the output voltage increases with V_e, but its growth rate gradually declines.

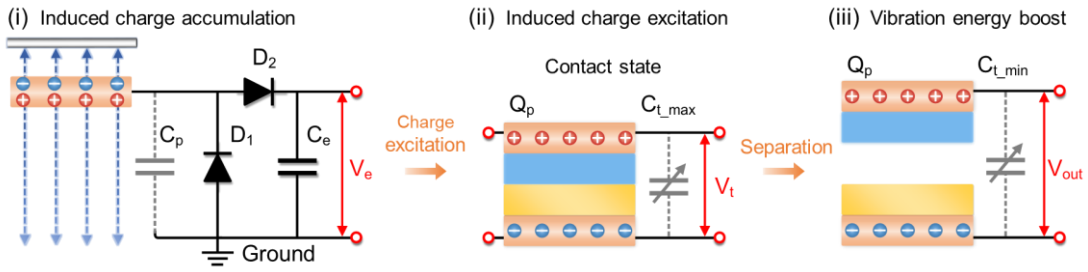

Figure N3. The theoretical relationship between the output voltage and excitation voltage.

Note S4 Charge decay in TENG-electrodes due to dielectric charge leakage and energy conversion efficiency of TENG

In the ICE-EVH system, TENG functions as a parallel-plate capacitor. When induced charges are pumped into TENG, a potential difference is established between the upper and bottom electrodes (Fig. N4A). When switch S_1 opens, the charge quantity and the voltage of C_t gradually decrease due to the leakage current between TENG-electrodes (Fig. N4B). Charge decay is a common challenge in charge-excitation-based TENGs, which can be mitigated by choosing appropriate dielectric films and reducing the dielectric charge leakage.[3] However, the charge decay in ICE-EVH is more severe than that in previous works due to the distinct energy transfer process and a much higher excitation voltage.[16-18] For example, at the contact state, the charge decay rate reaches 13.7% within one second (Fig. N4C). A more effective approach to suppress charge decay is required.

Increasing the vibration frequency f_v of TENG is an effective approach to reduce charge decay. As the vibration frequency of TENG increases, the time for each cycle shortens, which reduces the charge decay per cycle (Fig. N4D). Consequently, with the increase in vibration frequency, the output voltage of the ICE-EVH gradually increases (Fig. 3B in the manuscript).

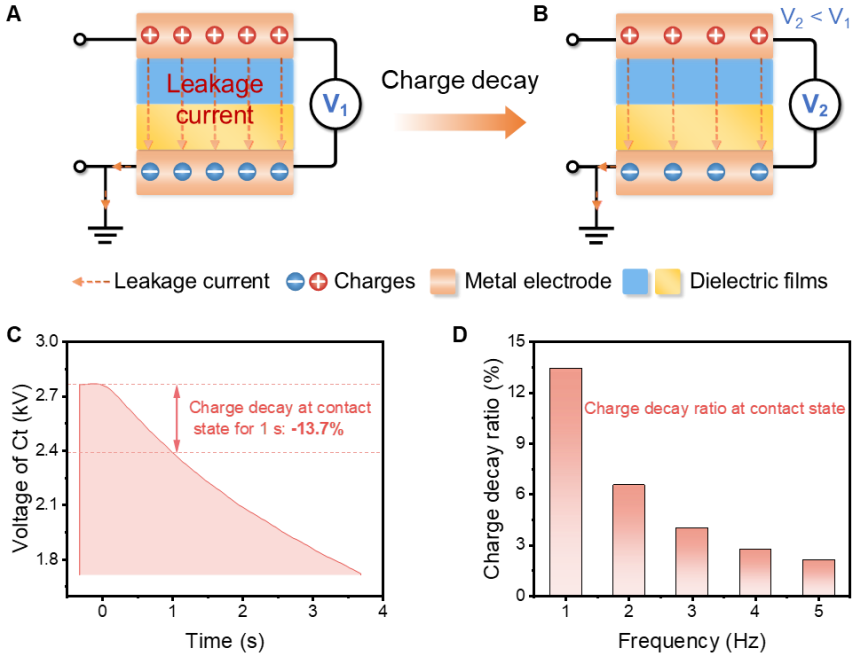

Figure N4. Charge decay in TENG-electrodes due to dielectric charge leakage.
(A)–(B) Schematic diagram of leakage current and charge decay in TENG-electrodes.
(C) Gradually decreased voltage of C_t due to charge decay.
(D) Less charge decay ratio at higher vibration frequencies.

Furthermore, the energy conversion efficiency of TENG was investigated. Although charge decay occurs during the operation of ICE-EVH, TENG still maintains a high energy conversion efficiency. For example, at a vibration frequency of 5 Hz, the output voltage is improved from 2.8 kV to 9.2 kV, representing a 3.3-fold enhancement.

The efficiency of TENG mainly depends on the energy conversion efficiency of

mechanical energy. As shown in Fig. N5A, the energy conversion efficiency of TENG can be calculated as:

$$\eta = \frac{E_{\text{out}}}{E_{\text{in1}} + E_{\text{in2}}} \times 100\% \tag{N5}$$

where E_{in1} and E_{in2} represent the input energy from the electric field and vibration, respectively, while E_{out} denotes the output energy. These energies are calculated as:

$$E_{\text{in1}} = 0.5 \times \frac{{Q_{\text{p}}}^2}{C_{\text{t\_max}}} \tag{N6}$$

$$E_{\text{in2}} = 0.5 \times {Q_{\text{p}}}^2 (\frac{1}{C_{\text{t\_min}}} - \frac{1}{C_{\text{t\_max}}}) \tag{N7}$$

$$E_{\text{out}} = 0.5 \times Q_{\text{out}} \times V_{\text{out}} \tag{N8}$$

where Q_{p} is the pumped induced charges per cycle, and Q_{out} is the charges stored in TENG at the separation state. Q_{out} is smaller than Q_{p} due to the charge decay.

At a vibration frequency of 3 Hz, Q_{p} is approximately 1090 nC. At a separation distance of 3 mm, $C_{\text{t\_min}}$ is about 65-79 pF (The parasitic capacitance at the separation state is very small, leading to measurement errors). The charge Q_{out} stored in TENG at separation state can be roughly estimated by integrating the discharge current curve in Fig. S21C. However, due to charge loss during the spark discharge of S_2, the calculated Q_{out} is lower than the actual value. At 3 Hz, Q_{out} is approximately 850 nC (Fig. N5B). Consequently, the energy conversion efficiency of TENG can be calculated as:

$$\eta = \frac{E_{\text{out}}}{E_{\text{in1}} + E_{\text{in2}}} \approx 36.7\%\sim44.7\% \tag{N9}$$

Notably, due to the measurement errors in $C_{\text{t\_min}}$ and Q_{out}, the actual efficiency may deviate from the calculated value. The main energy loss in TENG results from the charge decay. Higher vibration frequencies reduce charge decay and increase the output energy. For example, at a vibration frequency of 5 Hz, the output voltage is increased to 9.2 kV, which is much higher than 3 Hz. Consequently, the energy conversion efficiency of TENG will be further enhanced at higher vibration frequencies.

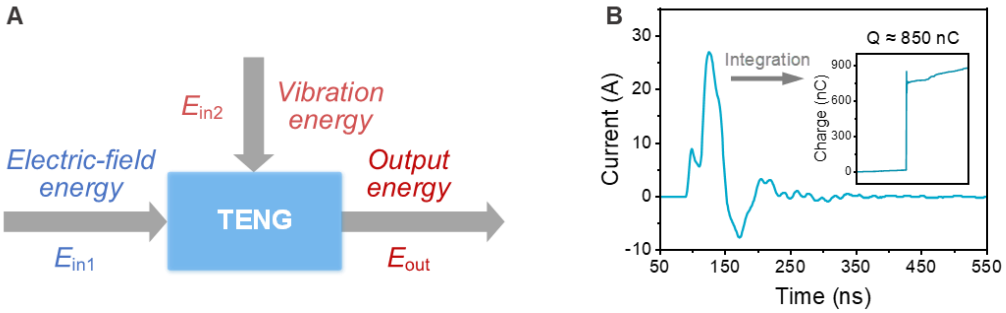

Figure N5. Efficiency of TENG.
(A) Energy transfer process in the TENG system.
(B) Discharge current and output charge curves at 3 Hz.

Note S5 Improving insulation performance of TENG-electrodes through structure optimization.

The insulation performance of a TENG is primarily determined by the output voltage and electric field distribution of the metal electrodes. At the same output voltage, higher electric field inhomogeneity increases the possibility of electrostatic breakdown between electrodes. Notably, breakdown primarily occurs at the metal electrode edges where the electric field inhomogeneity is highest.[19-21] To enhance the insulation performance of TENG we optimized the electrode structure systematically.

First, an additional dielectric film (PVDF) is attached to the bottom metal electrode, changing the typical three-layer structure to a four-layer one (Fig. N6A i). The four-layer structure (metal–dielectric film–dielectric film–metal) prevents direct contact between the upper dielectric film and the bottom metal electrode, significantly improving the insulation performance. Second, to reduce the electric field inhomogeneity at the electrode edges, a round-cornered rectangular electrode was used instead of a sharp-edged one (Fig. N6A ii and Fig. N6B–C).[6] Finally, an asymmetric upper and bottom electrodes was adopted instead of a symmetric design (Fig. N6A iii). As shown in Fig. S9, the bottom electrode (135 mm×92 mm) is slightly smaller than the upper one (140 mm×93.5 mm). Consequently, the distance between the edges of the upper and bottom electrodes at contact state is increased compared to the symmetric design, further reducing electric field inhomogeneity at the electrode edges (Fig. N6D-E). These structure optimizations significantly improved the insulation performance of the TENG electrodes (over 10 kV) and effectively reduce electrostatic breakdown during operation.

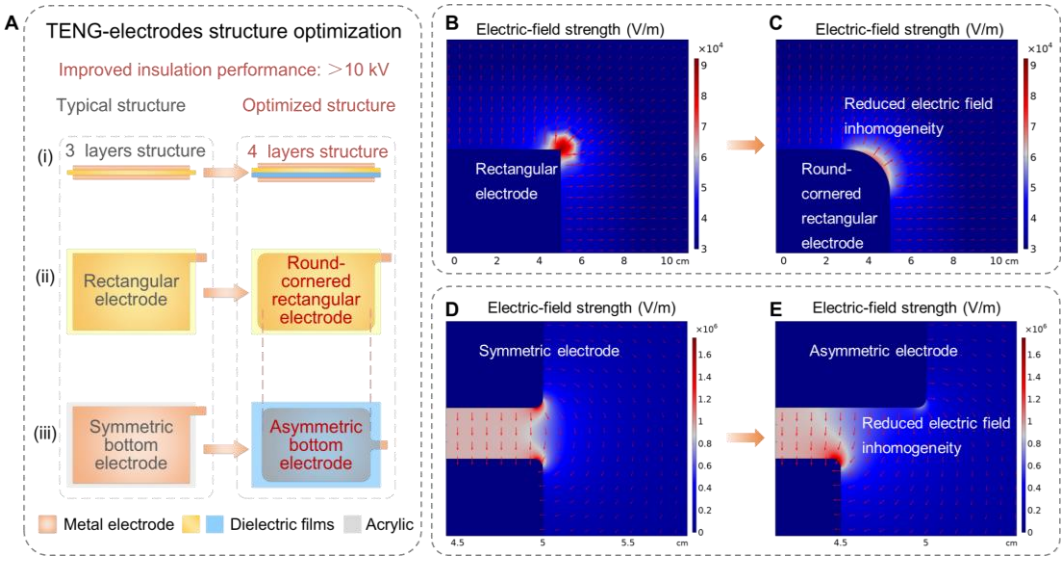

Figure N6. Improving insulation performance of TENG-electrodes through structure optimization. (A) Schematic diagram of TENG-electrodes before and after optimization. (B)–(C) Electric-field strength distribution at the edges of the rectangular and round-cornered-rectangle TENG-electrodes. (D)–(E) Electric-field strength distribution at the electrodes gap of symmetric and asymmetric TENG-electrodes.

Note S6 Optimal capacitance range for C_e.

In the working environment of power transmission lines, the frequency of mechanical vibration is typically below 10 Hz,[22-24] which is much smaller than the frequency of the AC electric field (Fig. N7A). Without C_e, the frequency mismatch between the TENG's vibration and the AC electric field would result in a portion of induced charges being "wasted" (Fig. N7B), reducing the charge utilization efficiency. After implementing C_e, the induced charges generated by the pump-electrode can be accumulated in C_e before being pumped into the TENG-electrodes (Fig. N7A), thus significantly improving the utilization efficiency of induced charges.

The amount of charge Q_2 stored in C_e during each cycle can be calculated as:

$$Q_2 = \frac{C_e Q}{C_p + C_e} \tag{N10}$$

where Q is the short-circuit transferred charge of EEH.

To ensure a high induced charge utilization efficiency (e.g., greater than 90%), the condition $C_e/(C_e+C_p) > 90\%$ should be satisfied. As a result, the capacitance of C_e should be at least 10 times that of C_p (typically below 100 pF). However, an excessively large C_e would lead to a slow voltage charging rate and a low excitation voltage (Fig. N7C), which will also result in a low output performance.

To determine the optimal range for C_e, the output voltage waveforms at different capacitances were measured (see Fig. 3D in the manuscript). The ICE-EVH exhibited optimal output performance at capacitances ranging from 470 pF to 10 nF (Fig. N7D).

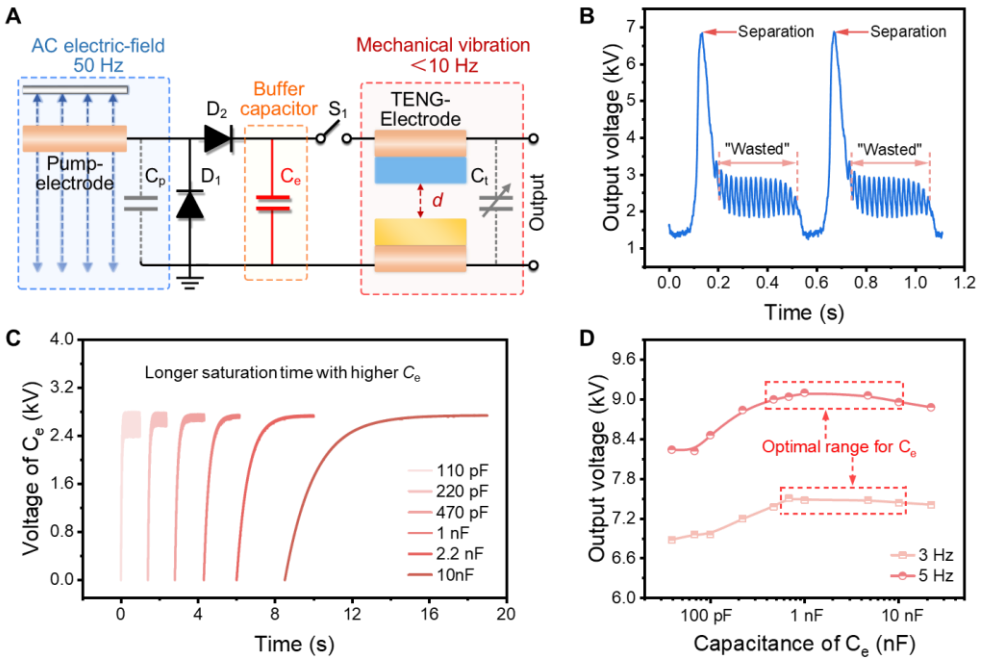

Figure N7. Optimal capacitance range for C_e. (A) Circuit diagram of ICE-EVH. (B) Output voltage of ICE-EVH without C_e. The switch S_1 maintains closed to display the output waveform of the EEH without C_e. (C) Capacitor charging curves for C_e. (D) Optimal capacitance range for C_e.

Note S7 Influence of environmental conditions on the performance of ICE-EVH.

As elaborated in Section 2.2-2.3 in the manuscript, the output of ICE-EVH is determined by the outputs of EEH and TENG. The output of EEH depends on the parasitic capacitance C_q between the pump-electrode and the transmission line, as well as the operating voltage U_L of the transmission line (Note S1). Once the position of the pump-electrode is fixed, external environmental factors have little impact on the parasitic capacitance and U_L. Therefore, the external environment factors have a negligible effect on EEH's output,[1,2] but they may influence the performance of ICE-EVH to some extent by affecting TENG's output.

In the real-world environment of high-voltage power equipment, key external factors that may affect the performance of ICE-EVH include temperature, humidity, and rain. To investigate these effects, an experimental platform was designed to simulate these conditions (Fig. N8A–B). In the experiments, the humidity in the TENG-electrodes' working environment was controlled using a humidifier and a dehumidifier (Fig. N8A). To evaluate the impact of temperature, the TENG-electrodes were preheated to the rated temperature before measuring the output voltage. To simulate rainfall, a water tank with perforations at the bottom was placed above the ICE-EVH prototype (Fig. N8B).

Fig. N8C–D presents the output voltage of ICE-EVH at different temperatures. In the working environment of overhead transmission lines, temperature typically remains below 50°C, within which the output voltages exhibit minimal variations. At 60°C, the output decreases slightly to 8.6 kV, which is likely due to the increased leakage current and reduced relative permittivity of the dielectric film at high temperature conditions. These results demonstrate that the ICE-EVH maintains stable performance under typical temperature variations. In higher-temperature environments, employing dielectric films with better thermal stability can ensure stable output performance.[25]

Humidity also influences the output of ICE-EVH. As humidity rises from 10% to 50%, the output voltage decreases slightly from 9.1 kV to 8.8 kV (Fig. N8E–F). With further increases in humidity, the decline becomes more pronounced. At 80% humidity, the output voltage decreases to 7.6 kV, representing a 16% reduction. This reduction is likely due to higher leakage current, as water molecules accumulate on the dielectric films of the TENG-electrodes in high humidity conditions. However, the TENG-electrodes in the actual ICE-EVH prototype are enclosed within the shell, which helps mitigate the impact of external humidity greatly.

Furthermore, the effect of rain was investigated. Raindrops do not cause any observable change in the output of EEH (Fig. N8G). Additionally, the TENG-electrodes in the actual ICE-EVH prototype are enclosed within the shell, isolating them from rain. As a result, exposure to rain has a negligible effect on the system's stability (Fig. N8H).

Overall, while environmental factors such as high temperature and humidity may influence the output of ICE-EVH, its performance remains relatively stable under typical environmental variations.

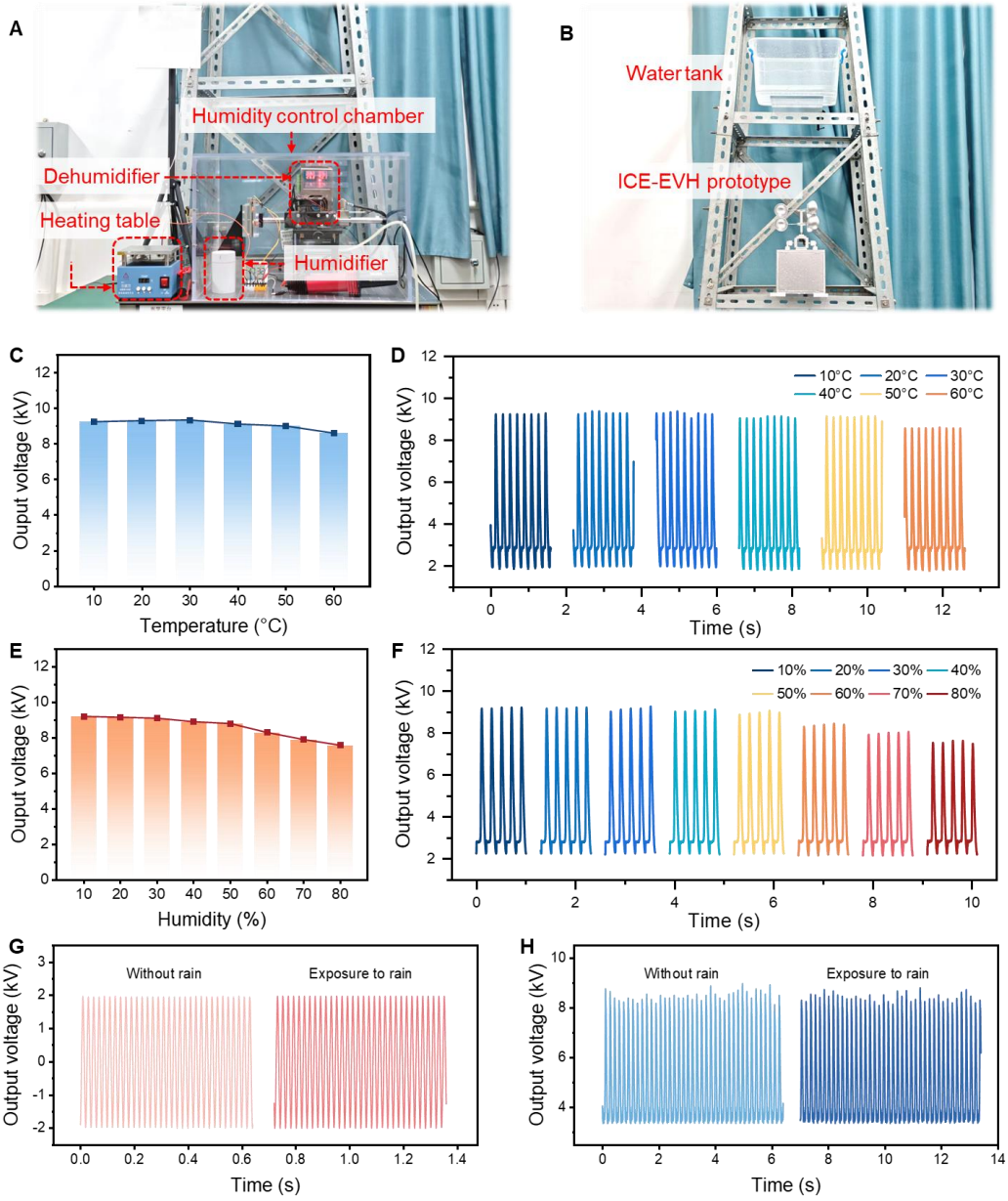

Figure N8. The effects of wind and rain on the output performance.

(A)–(B) Photographs of the experimental platform.

(C) Effect of temperature.

(D) Output voltage curves at different temperatures.

(E) Effect of humidity.

(F) Output voltage curves at different humidities.

(G) Output voltage curves of the pump-electrode in the ICE-EVH prototype.

(H) Output voltage curves of the ICE-EVH prototype.

Note S8 Energy conversion efficiency of the proposed power management circuit.

The energy conversion efficiency of the power management circuit (PMC) determines the output power of ICE-EVH. We investigated the energy conversion efficiency of the proposed PMC by calculating the input and output power, and enhanced the efficiency by optimizing circuit parameters.

The input power of the PMC depends on the energy released per cycle through switch S_2 and the vibration frequency f_v. At a frequency of 5 Hz, the energy E_{in} input to the PMC is approximately 3.78 mJ per cycle (see Fig. 4J in the manuscript). Therefore, the input power of the PMC is:

$$P_{in} = \frac{E_{in}}{T} = \frac{3.78\ \text{mJ}}{0.02\ \text{s}} \approx 18.9\ \text{mW} \quad \text{(N11)}$$

Consequently, the energy conversion efficiency η of the PMC can be calculated as:

$$\eta = \frac{P_{out}}{P_{in}} \times 100\% = \frac{13.2\ \text{mW}}{18.9\ \text{mW}} \times 100\% \approx 70\% \quad \text{(N12)}$$

The energy conversion efficiency of the PMC mainly depends on the inductor L and the freewheeling diode D_3.[1,8] Using a freewheeling diode with a low forward voltage reduces losses and enhances the efficiency. In this PMC, the main energy loss may result from the inductor L. Since the short-circuited current of S_2 exceeds 30 A, a portion of the magnetic field energy is lost in the inductor due to the magnetic saturation. To improve the output power, we compared the output power with various inductors. Results indicate that the highest output power is achieved with six 1 mH inductors connected in series (each 10 mm × 12 mm in size) (Fig. N9A–B).

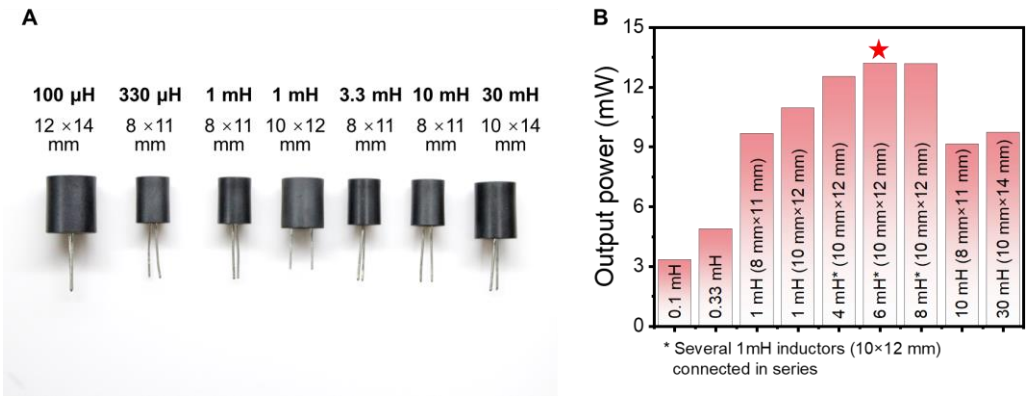

Figure N9. Energy conversion efficiency of the proposed power management circuit.
(A) Photograph of different inductors.
(B) Output power of the PMC with different inductors.

Note S9 Enhanced energy conversion efficiency and output power by stacked TENG-electrodes.

In the actual ICE-EVH prototype, the parasitic capacitance of TENG-electrodes is relatively small (~2 nF), and the excitation voltage V_e is high (~3.5 kV). A smaller C_t and a higher V_e result in more severe charge decay. Consequently, increasing V_e from 1200 V to 3500 V resulted in a slight increase in output voltage (Fig. N10A), indicating significant energy loss at high V_e.

To enhance energy conversion efficiency and improve the performance of the ICE-EVH prototype, an optimized stacked TENG-electrodes design was implemented. By utilizing multiple parallel-connected TENG-electrodes, the excitation voltage distributed to each TENG-electrodes is reduced, thereby minimizing the charge decay and enhancing overall performance. This enhancement can be intuitively illustrated by the voltage–charge plot. After implementing power management, the ideal voltage–charge plot of ICE-EVH is a right-angled triangle, where the enclosed area represents the output energy.

As shown in Fig. N10B, with a single pair of TENG electrodes (TE), the output energy is significantly lower than the theoretical maximum due to severe charge decay. Achieving high output energy requires both a high output voltage and a large output charge with minimal charge decay. Implementing stacked TENG-electrodes reduces the excitation voltage distributed to each TENG-electrodes, thereby mitigating charge decay. Fig. N10C–D presents the output voltages for various numbers of TENG-electrode pairs. With four TENG-electrodes pairs, each pair shares an excitation voltage of roughly 1 kV, resulting in an output voltage of about 7.7 kV. The corresponding voltage–charge plot is shown in Fig. N10E. The output voltage is slightly lower than that of a single TENG-electrode pair. However, due to the substantially reduced excitation voltage and charge decay, the overall output energy is enhanced significantly.

However, as shown in Fig. N10D, when the number of TENG-electrodes pairs increases to six, the output voltage decreases significantly to approximately 5.8 kV. This reduction may result from the lower excitation voltage per TENG-electrodes pair. Lower output voltages also decrease the output energy. According to Fig. N10A, to achieve a high output voltage and minimal charge decay, the excitation voltage per TENG-electrodes pair should be maintained within 0.8–1.1 kV. Therefore, in this study, four pairs of stacked TENG-electrodes were employed.

Further, the durability of the ICE-EVH prototype as well as the stacked TENG-electrodes were investigated. After operating continuously for about 3.5 hours, the output performance of all four pairs of TENG-electrodes shows no observable decay, indicating good durability (Fig. N10G). The fluctuations in the voltage result from the wind speed variations and mechanical inconsistencies caused by the manually fabricated rocker arm in the prototype, which intermittently affect the stability of vibration. These instabilities can be mitigated through refined structural design and precision manufacturing in practical applications.

In summary, these experimental results validate that stacked TENG-electrodes is an effective approach to increase the output power of the prototype in practical

applications, offering both good scalability and durability.

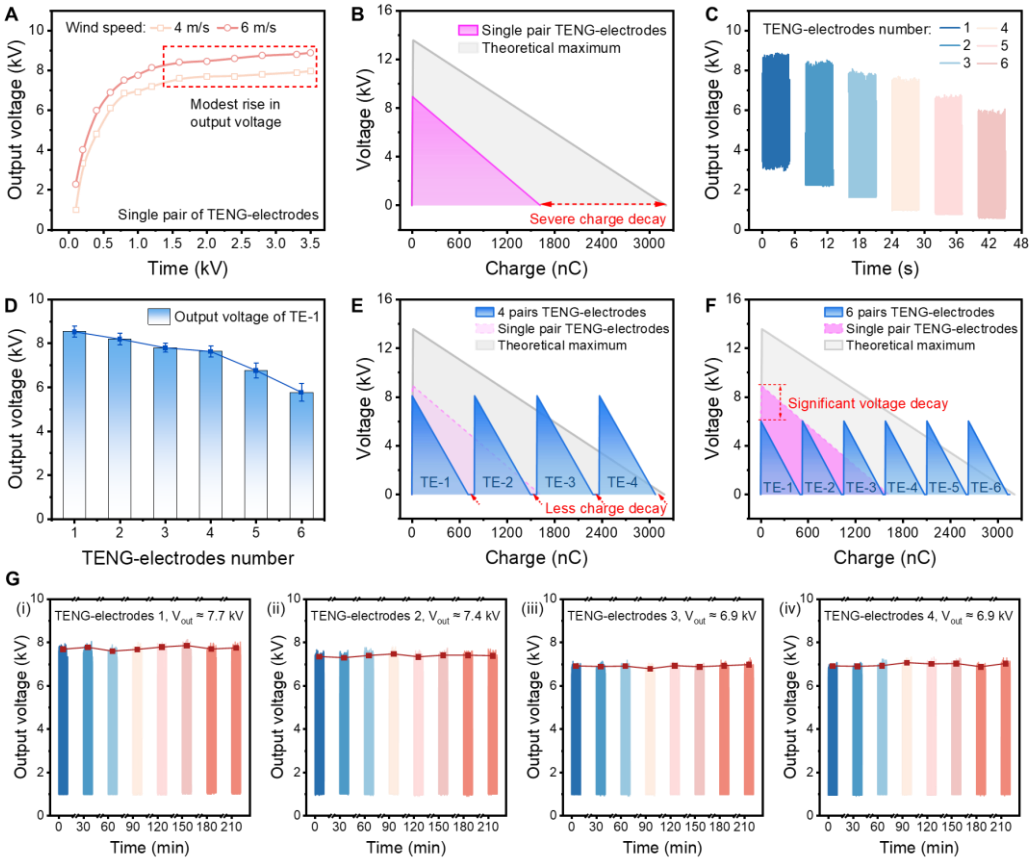

Figure N10. Enhanced energy conversion efficiency and output power by stacked TENG-electrodes.

(A) Output voltage of the ICE-EVH prototype at different excitation voltages.

(B) Simulated voltage–charge plot of a single TENG-electrodes pair.

(C)–(D) Output voltages with increasing numbers of TENG-electrodes pairs.

(E)–(F) Simulated voltage–charge plots for stacked TENG-electrodes.

(G) Durability test for stacked TENG-electrodes.

Each pair of electrodes operated continuously for about 3.5 hours, during which the output voltage waveform was measured every 0.5 hours.

Supplementary References

1. D. Hu, Q. Wang, D. Zheng, X. Huang, Z. Wu, F. Wang, S. Xu and S. Chen, *Nano Energy*, 2024, **131**, 110197.
2. X. J. Zeng, Z. T. Yang, P. F. Wu, L. Y. Cao and Y. P. Luo, *IEEE Trans. Ind. Electron.*, 2021, **68**, 7083-7092.
3. J. Wang, B. Zhang, Z. Zhao, Y. Gao, D. Liu, X. Liu, P. Yang, Z. Guo, Z. L. Wang and J. Wang, *Adv. Energy Mater.*, 2024, **14**, 2303874.
4. Z. Guo, P. Yang, Z. Zhao, Y. Gao, J. Zhang, L. Zhou, J. Wang and Z. L. Wang, *Energy Environ. Sci.*, 2023, **16**, 5294-5304.
5. L. Zhou, H. Liu, K. Zuo and K. Shang, *High Voltage*, 2024, **9**, 816-825.
6. Z. Wang, W. L. Liu, W. C. He, H. Y. Guo, L. Long, Y. Xi, X. Wang, A. P. Liu and C. G. Hu, *Joule*, 2021, **5**, 441-455.
7. Y. Gao, D. Liu, Y. Li, J. Liu, L. Zhou, X. Li, Z. Zhao, S. Li, P. Yang, Z. L. Wang and J. Wang, *Energy Environ. Sci.*, 2023, **16**, 2304-2315.
8. Z. Wang, Q. Tang, C. C. Shan, Y. Du, W. C. He, S. K. Fu, G. Li, A. P. Liu, W. L. Liu and C. G. Hu, *Energy Environ. Sci.*, 2021, **14**, 6627-6637.
9. Z. Cao, J. Teng, R. Ding, J. Xu, C. Ren, S.-H. Lee, X. Guo and X. Ye, *Energy Environ. Sci.*, 2024, **17**, 5002-5012.
10. G. Cheng, Z.-H. Lin, L. Lin, Z.-l. Du and Z. L. Wang, *Acs Nano*, 2013, **7**, 7383-7391.
11. G. C. Shen, Y. L. Hu, J. P. Li, J. M. Wen and J. J. Ma, *Energy Conv. Manag.*, 2023, **292**, 117368.
12. D. Y. Hu, X. L. Huang, D. P. Zheng, Z. F. Wu, C. M. Ding, F. Wang, S. X. Xu and S. Chen, *Nano Energy*, 2024, **119**, 109077.
13. C. M. Bao, H. Y. Dan, M. Y. Zhang, C. B. Li, Z. L. Wang and Y. Yang, *Nano Energy*, 2023, **106**, 108063.
14. C. Ye, D. Liu, P. Chen, L. N. Y. Cao, X. Li, T. Jiang and Z. L. Wang, *Adv. Mater.*, 2023, **35**, 2209713.
15. S. Liu, X. Liang, J. Han, Y. Duan, T. Jiang and Z. L. Wang, *Applied Physics Reviews*, 2024, **11**.
16. H. Wang, L. Xu, Y. Bai and Z. L. Wang, *Nat. Commun.*, 2020, **11**, 4203.
17. L. Xu, T. Z. Bu, X. D. Yang, C. Zhang and Z. L. Wang, *Nano Energy*, 2018, **49**, 625-633.
18. W. Liu, Z. Wang, G. Wang, G. Liu, J. Chen, X. Pu, Y. Xi, X. Wang, H. Guo, C. Hu and Z. L. Wang, *Nat. Commun.*, 2019, **10**, 1426.
19. Y. Gao, L. He, D. Liu, J. Zhang, L. Zhou, Z. L. Wang and J. Wang, *Nat. Commun.*, 2024, **15**, 4167.
20. J. R. Riba, *Eur. J. Phys.*, 2024, **45**, 045205.
21. H. Kojima, K. Hotta, T. Kitamura, N. Hayakawa, A. Otake, K. Kobayashi, T. Kato, T. Rokunohe and H. Okubo, *IEEE Trns. Dielectr. Electr. Insul.*, 2016, **23**, 194-201.
22. H. Wu, J. Y. Wang, Z. Y. Wu, S. L. Kang, X. L. Wei, H. Q. Wang, H. Luo, L. J. Yang, R. J. Liao and Z. L. Wang, *Adv. Energy Mater.*, 2022, **12**, 2103654.
23. X. Zhang, Y. Yu, X. Xia, W. Zhang, X. Cheng, H. Li, Z. L. Wang and T. Cheng, *Adv. Energy Mater.*, 2023, **13**, 2302353.
24. L. Wang, Y. Zhang, X. Zhang, X. Cheng, S. Zhai, X. Bi, H. Li, Z. Wang and T. Cheng, *Adv. Energy Mater.*, 2024, **15**, 2403318.
25. Y. Liu, J. Wang, T. Liu, Z. Wei, B. Luo, M. Chi, S. Zhang, C. Cai, C. Gao and T. J. N. C. Zhao, *Nat. Commun.*, 2025, **16**, 383.